Validity of mean-field theory in a dissipative critical system: Liouvillian gap, $\mathbb{PT}$-symmetric antigap, and permutational symmetry in the *XYZ* model

Dolf Huybrechts,[1,*] Fabrizio Minganti,[2,†] Franco Nori,[2,3,‡] Michiel Wouters,[1,§] and Nathan Shammah[2,4,‖]

[1]*Theory of Quantum & Complex Systems, University of Antwerp, B-2610 Wilrijk, Belgium*

[2]*Theoretical Quantum Physics Laboratory, RIKEN Cluster for Pioneering Research, Wako-shi, Saitama 351-0198, Japan*

[3]*Physics Department, The University of Michigan, Ann Arbor, Michigan 48109-1040, USA*

[4]*Quantum Technology Lab, Dipartimento di Fisica, Università degli Studi di Milano, 20133 Milano, Italy*

(Received 2 January 2020; revised manuscript received 18 March 2020; accepted 1 May 2020; published 1 June 2020)

We study the all-to-all connected *XYZ* (anisotropic-Heisenberg) spin model with *local and collective* dissipations, comparing the results of mean-field (MF) theory with the solution of the Lindblad master equation. Exploiting the weak $\mathcal{PT}$ symmetry of the model (referred to as Liouvillian $\mathbb{PT}$ symmetry), we efficiently calculate the Liouvillian gap, introducing the idea of an *antigap*, and we demonstrate the presence of a paramagnetic-to-ferromagnetic phase transition. Leveraging the permutational symmetry of the model [N. Shammah *et al.*, Phys Rev. A **98**, 063815 (2018)], we characterize criticality, finding exactly (up to numerical precision) the steady state for N up to $N = 95$ spins. We demonstrate that the MF theory correctly predicts the results in the thermodynamic limit in all regimes of parameters, and quantitatively describes the finite-size behavior in the small anisotropy regime. However, for an intermediate number of spins and for large anisotropy, we find a significant discrepancy between the results of the MF theory and those of the full quantum simulation. We also study other more experimentally accessible witnesses of the transition, which can be used for finite-size studies, namely, the bimodality coefficient and the angular-averaged susceptibility. In contrast to the bimodality coefficient, the angular-averaged susceptibility fails to capture the onset of the transition, in striking difference with respect to lower-dimensional studies. We also analyze the competition between local dissipative processes (which disentangle the spin system) and collective dissipative ones (generating entanglement). The nature of the phase transition is almost unaffected by the presence of these terms. Our results mark a stark difference with the common intuition that an all-to-all connected system should fall onto the mean-field solution also for intermediate number of spins.

DOI: 10.1103/PhysRevB.101.214302

I. INTRODUCTION

Many-body quantum physics with light and matter is at the center of intense research, being at the crossroad of condensed matter, statistical mechanics, quantum optics, and quantum information. In these open quantum systems, excitations, energy, and coherence are continuously exchanged with the environment, and they can be driven via pumping mechanisms [1–3]. Experimentally, light-matter interactions can be studied using Rydberg atoms confined between high-quality mirrors [1], superconducting circuits [4,5], semiconductor cavities [6–8], and optomechanical systems [9]. In many of these setups, a key role is played by the "photons," that is, electromagnetic field excitations dressed by the matter degrees of freedom, thus permitting a finite effective photon-photon interaction (e.g., the polariton [10–12]).

The experimental advances of the last decade provided the opportunity to realize extended lattices of resonators, allowing to explore criticality in this out-of-equilibrium context. While quantum or thermal phase transitions can be determined by (free-)energy analysis [13,14], their dissipative counterparts need not to obey the same paradigm [15–20], and by properly designing the coupling with the environment and the driving mechanisms, it is possible to stabilize phases without an equilibrium counterpart [21–27]. There exist a plethora of theoretical examples discussing the emergence of such dissipative phase transitions for photonic systems [28–42], lossy polariton condensates [43–45], and spin models [15,25,27,46–56]. Moreover, some key experiments proved the validity of the theoretical predictions in single superconducting cavities [57] and lattices of superconducting resonators [58,59], Rydberg atoms in optical lattices [60,61], optomechanical systems [9,62], exciton-polariton condensates [12,63], and semiconductor micropillars [64,65].

In particular, the competition between interaction, driving, and dissipation processes can lead to exotic physics, such as a transition from a photonic Mott insulator to a superfluid phase [66–70], similar to that observed with ultracold atoms confined in optical lattices [71,72]. Moreover, in the limit of a very strong nonlinearity one enters the regime of *photon*

*dolf.huybrechts@uantwerpen.be
†fabrizio.minganti@riken.jp
‡fnori@riken.jp
§michiel.wouters@uantwerpen.be
‖nathan.shammah@gmail.com; current address: Unitary Fund (https://unitary.fund/).

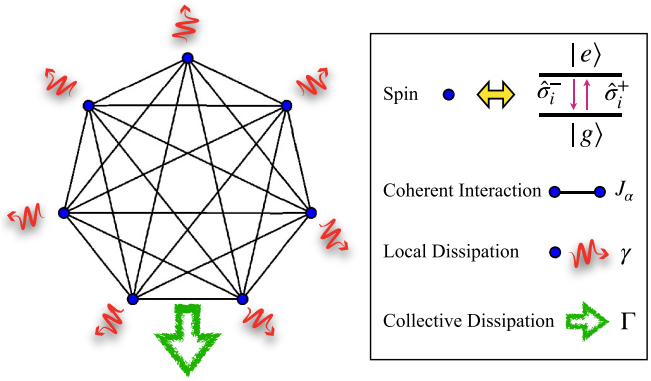

FIG. 1. Sketch of the dissipative *XYZ* model, with local and collective dissipation. In the legend we illustrate the possibility of implementing the spin model on an ensemble of two-level systems, or (artificial) atoms, interacting with an electromagnetic field. Each two-level system can switch between a ground $|g\rangle$ and excited state $|e\rangle$. While the spin-spin interactions, $\propto J_\alpha$, of the all-to-all connected lattice can be mediated by the coherent interaction with the photonic field, its collective mode dissipates, at a rate $\propto \Gamma$, and all other spin-flip mechanisms contribute to local dissipation, $\propto \gamma$.

blockade [73–76], where the presence of two photons inside the cavity becomes practically impossible. This effect has been observed experimentally both in a single atom in a cavity [77] and in a single superconducting circuit [78]. Interestingly, a system of coupled superconducting resonators [58,68,79–81] or Rydberg atoms [48,82–86] can be mapped onto an effective spin model, as sketched in Fig. 1.

In this regard, the *XYZ* Heisenberg model describes, with a high degree of generality, these systems and other spin models. In the dissipative *XYZ* model, each spin interacts with its nearest neighbors via an anisotropic Heisenberg Hamiltonian. Moreover, each spin is coupled to the environment inducing random spin flips in the z-axis direction. Due to its relative generality and simplicity, this model has been taken both as an example of a system exhibiting dissipative phase transitions, as well as a benchmark to test numerical methods. Indeed, a single-site Gutzwiller mean-field (MF) theory can already retrieve a rich phase diagram for this model [25]. Numerical studies, capable of including long-range correlations, have confirmed a critical behavior in two-dimensional lattices and the absence of criticality in one dimension (1D) [27,38,52,55,87–89]. Notwithstanding the fact that a collective bosonic field can be mapped onto an all-to-all-connected spin system [90], we emphasize that the rich *XYZ* model phase diagram in different regimes is a cornerstone of the study of many-body spin quantum systems, magnetism, spin dynamics, and quantum phase transitions [86]. Indeed, it is the most general case of the Ising model and of the *XXZ* model, of the Lipkin-Meshkov-Glick model and other spin-squeezing Hamiltonians, to which it can fall onto, for the appropriate choice of parameters [49].

This work

In this paper, we investigate the properties of an all-to-all (or fully) connected dissipative *XYZ* system. The interest and purpose of this study is manifold:

(i) In the general study of a quantum system, one can think of the all-to-all connected model with uniform coupling as one in which long-range correlations cannot take place since all sites are at distance one. In this regard, it is "common wisdom" that a high-dimensional large system should recover the results of the mean-field prediction. Even if this can be argued for thermodynamic systems (where Landau-Ginzburg theory can be applied to determine phase transitions [91]), the lack of free-energy analysis does not allow such an easy argument in open quantum systems. We will consider the simplest type of nonthermal bath to try to address this question.

(ii) Even if the mean field were to work, it should be predictive only in the thermodynamic limit. What is not clear is how the system behavior scales up to the infinite spin number. The high degree of symmetry of the all-to-all connected system allows for a dramatic reduction of the computational cost of the numerical calculations [92]. Moreover, many atoms-in-cavity experiments can be recast as all-to-all connected models by the mediation of the electromagnetic field, which collectively interacts with the atoms [90]. However, since in these systems there is a limited number of particles, identifying the correct observables to characterize the emergence of the phase transition is of paramount importance. We provide a thorough study of the spin-structure factor, the collective magnetization, the bimodality coefficient, and the angular-averaged susceptibility. We also characterize less experimentally accessible quantities signaling the phase transition, as the von Neumann entropy of the steady state and the Liouvillian spectrum and its gap. We test which one fares better in this intermediate regime to capture the onset of criticality.

(iii) The permutational method which we use here is exact (that is, no approximation on the model has been done). Exact computations on open-spin systems have been carried out for systems up to 16 spins [55]. This paper pushes this boundary far beyond this limit.

The all-to-all connected geometry under consideration constitutes also an ideal benchmark for linked-cluster expansion theories [93]. In this kind of approach, one develops a perturbation expansion in power series of the coordination number around the Gutzwiller (or atomic) MF limit of a lattice model [94]. In the limit of weak spatial fluctuation, the effect of correlations is known to produce a correction scaling as the inverse of the coordination number to the Gutzwiller mean-field limit, and therefore MF results are expected to be exact [95,96]. As pointed out in Ref. [97], however, around second-order critical points correlations diverge, and higher-order correlation schemes should be taken into consideration to properly capture criticality.

Finally, we also stress that linked-cluster expansions explicitly deal with infinite lattice size, while our study is a finite-size one. Moreover, in our lattice, the ratio between the number of sites and the dimension of the lattice N/d is of order one for large lattices, while in the usually defined thermodynamic limit, the number of sites diverges with respect to the dimension.

1. Original results

Our extensive investigations of various thermodynamic properties of the all-to-all dissipative *XYZ* model are made

possible by the use of permutational symmetry in Liouvillian space [92] and are relevant for state-of-the-art noisy quantum simulators. The original results obtained in this paper are as follows:

(i) We derive the phase diagram from mean-field and quantum steady-state solutions, as well as from the study of the Liouvillian gap. We find the absence of an antiferromagnetic phase and only one phase transition, from a paramagnetic to a ferromagnetic phase.

(ii) Additionally, we exploit the $\mathbb{PT}$ symmetry of Liouvillians [98] emerging in spin models whose Hamiltonian has an all-to-all interaction, and the Lindbladian part introduces homogeneous local dissipation processes. We introduce an efficient method to calculate the Liouvillian gap, whose closing marks a dissipative phase transition in the thermodynamic limit, from its symmetric *antigap*, which, as we detail, can be numerically computed much more easily. We provide a general description of this technique since it may be applied to the study of other models.

(iii) We show that the full quantum Lindblad dynamics converges, with a power-law behavior, to the Gutzwiller mean-field steady-state predictions. In the highly anisotropic ferromagnetic regime, the discrepancy is much larger than in other regimes, even for $N \simeq 100$ spins; moreover, the convergence to the mean-field results is much slower with respect to the low-anisotropy ferromagnetic regime. In this regard, even though we do not find a second phase transition [27], we find that the high- and low-anisotropy regimes are profoundly different from one another.

(iv) In the presence of both local and collective dissipation, the phase transition is a second-order one, just like the case of local dissipation only (differently from the case of collective dissipation only [49]).

2. Paper structure

The paper is organized as follows: In Sec. II we introduce the spin model, also providing possible experimental implementations. In Sec. III we provide a description of the Liouvillian superoperator and its spectral properties. In Sec. III A we introduce the concept of Liouvillian antigap for $\mathbb{PT}$-symmetric Liouvillians. In Sec. III B we then compute the closing of the Liouvillian gap and its critical slowing down for the *XYZ* model with local dissipation. In Sec. IV we derive the mean-field equations, considering both the case of local and collective dissipation, and the well-studied case of local dissipation only, on which we focus for the main part of the subsequent analysis.

In Sec. V, we then compare the mean-field predictions, obtained from analytical solutions, to a numerical study of the quantum model, performed exploiting permutational symmetry, in the two qualitatively different regimes of the phase diagram: across criticality and for large anisotropy. In particular, in Sec. V A we study the properties of the phases across the critical region (paramagnetic phase, critical point, and ferromagnetic phase) comparing various quantities (spin-structure factor, magnetization, von Neumann entropy). In Sec. V B we focus on pinpointing the phase transition, introducing the bimodality coefficient and the angular-averaged susceptibility. In Sec. V C we characterize the region of high anisotropy. In Sec. V D, we consider the steady-state properties and phase transition in the presence of both local and collective dissipation. Finally, in Sec. VI we provide our concluding remarks.

The interested reader can find in the Appendices some general remarks as well as details about the techniques used to perform the numerical and MF analysis. In particular, in Appendix A we discuss in general the symmetries of Liouvillians, the properties of the Liouvillian spectrum, and the characterization of phase transitions in these systems; in Appendix C we highlight the properties of collective dissipation only and the connection of spin models with superradiant models in cavity-QED; in Appendix D we provide details on the use of permutational symmetry in Liouvillian space in the presence of homogeneous local dissipation; in Appendix E we provide a detailed definition of all the quantities used for the MF validity study.

II. MODEL

The Heisenberg model describes the physics of a d-dimensional lattice of spins or two-level systems, characterized by nearest-neighbors interaction. Its Hamiltonian reads as ($\hbar = 1$)

$$\hat{H} = \frac{1}{Z}\sum_{\langle i,j\rangle}\left(J_x\hat{\sigma}_i^x\hat{\sigma}_j^x + J_y\hat{\sigma}_i^y\hat{\sigma}_j^y + J_z\hat{\sigma}_i^z\hat{\sigma}_j^z\right), \tag{1}$$

where Z indicates the coordination number, $\langle i, j\rangle$ indicates the sum over nearest-neighbor links, J_α ($\alpha = x, y, z$) represent the coupling strengths of spin-spin interactions, $\hat{\sigma}_i^\alpha$ are the Pauli matrices of the ith spin. Since we consider $J_x \neq J_y \neq J_z$, we will refer to this anisotropic Heisenberg model as an *XYZ* model. If such a system weakly interacts with a Markovian environment, its dynamics is captured via a Lindblad master equation [1,2]. In the simplest model, the environment induces the system to relax in a preferential direction, e.g., aligning the spins along the z direction; this can occur with two qualitatively different mechanisms. The first one flips a single spin toward the negative direction of the z axis, with γ quantifying the rate of spin-flip processes. The second one characterizes the collective loss of one excitation at a rate Γ. The state of the system is thus captured by a density matrix $\hat{\rho}(t)$ evolving via

$$\frac{\partial\hat{\rho}(t)}{\partial t} = \mathcal{L}\hat{\rho}(t) = -i[\hat{H},\hat{\rho}(t)] + \gamma\sum_{j=1}^{N}\mathcal{D}[\hat{\sigma}_j^-]\hat{\rho}(t) + \frac{\Gamma}{N-1}\mathcal{D}\left[\sum_{j=1}^{N}\hat{\sigma}_j^-\right]\hat{\rho}(t), \tag{2}$$

where N is the number of two-level systems, $\hat{\sigma}_j^\pm = (\hat{\sigma}_j^x \pm i\hat{\sigma}_j^y)/2$ are the raising and lowering operators for the jth spin, $\mathcal{D}[\hat{A}]$ represents a Lindblad dissipator of the form

$$\mathcal{D}[\hat{A}]\hat{\rho}(t) = \hat{A}\hat{\rho}(t)\hat{A}^\dagger - \tfrac{1}{2}(\hat{A}^\dagger\hat{A}\hat{\rho}(t) + \hat{\rho}(t)\hat{A}^\dagger\hat{A}), \tag{3}$$

acting on the jth site, and $\mathcal{L}$ is the Liouvillian superoperator. These processes are sketched in Fig. 1.

Given a Lindblad master equation, a central role is played by the steady-state density matrix $\hat{\rho}_{\rm ss}$, which is the matrix

which does not evolve anymore under the action of the Lindblad master equation, i.e., $\partial_t \hat{\rho}_{ss} = \mathcal{L}\hat{\rho}_{ss} = 0$. For systems admitting a unique steady state (such as the *XYZ* for a finite number of sites), the steady state describes the system after its transient dynamics took place, and as such it corresponds to $\hat{\rho}(t \to \infty)$.

If we consider an all-to-all connected model with uniform couplings, i.e., all the spins interact with each other with the same strength, the Hamiltonian in Eq. (1) can be recast as

$$\hat{H} = \frac{1}{2(N-1)}[J_x(\hat{S}^x)^2 + J_y(\hat{S}^y)^2 + J_z(\hat{S}^z)^2], \tag{4}$$

where we have introduced the collective operators $\hat{S}^\alpha = \sum_{i=1}^{N} \hat{\sigma}_i^\alpha$ for $\alpha = x, y, z$. Notice the factor 2 is due to the fact that in Eq. (1) the sum is over the links while to obtain Eq. (4) we have to sum over the sites. Moreover, in the all-to-all connected model, the coordination number $Z = N - 1$. The collective dissipation becomes $\mathcal{D}[\sum_j \hat{\sigma}_j^-] = \mathcal{D}[\hat{S}^-]$, while the local dissipation cannot be recast in terms of a single collective operator. In this regard, in the all-to-all connected model, the Hamiltonian and collective dissipation processes will tend to create correlated states, while local dissipation will disentangle them.

However, it is commonly accepted that in a high-dimensional model $d \gg 1$, in the thermodynamic limit fluctuation is suppressed and the correct result should be captured by a mean-field decoupling procedure [46,47]. The resulting steady-state density matrix is a tensor product of identical local density matrices.

In this work, we will investigate the phase transition from a paramagnetic phase with no magnetization in the *xy* plane ($\langle\hat{\sigma}^x\rangle = \mathrm{Tr}\,[\hat{\rho}_{ss}\hat{\sigma}_j^x] = 0$, $\langle\hat{\sigma}^y\rangle = \mathrm{Tr}[\hat{\rho}_{ss}\hat{\sigma}_j^y] = 0$) to a ferromagnetic phase with finite magnetization in the *xy* plane ($\langle\hat{\sigma}^x\rangle \neq 0$, $\langle\hat{\sigma}^y\rangle \neq 0$) which is expected to happen in the thermodynamic limit of the *XYZ* model for anisotropic coupling $J_x \neq J_y$ [25,27,38,52,87–89]. Note that at $T = 0$ and in the absence of dissipation no quantum phase transition of this kind exists in this system.

Experimental implementations

We envision that the predictions that will be detailed hereafter can be observed in experiments with noisy quantum simulators and long-range interaction, based on a broad variety of platforms: atomic clouds [83], Rydberg atoms [48,50,82,84,86], trapped ions [99–102], as well as in solid state [103,104], e.g., in superconducting circuits [5,23,58,105–107] and especially in hybrid superconducting systems [108], where a bosonic field mediates the effective spin-spin interactions. Indeed, Ref. [86] shows the feasibility of investigating exactly the all-to-all connected *XYZ* model in Rydberg atoms. Probing the dissipative regime here studied only requires implementing a weak-coupling interaction with an additional cavity mode allowing for dispersive measurement of the radiated field. Trapped ions provide another platform on which to engineer long-range spin interactions [100–102] and already allow one to investigate dissipative phase transitions with tens of two-level systems, which can also be locally manipulated [109].

Superconducting circuit elements and condensed matter magnetic degrees of freedom can be plugged together to implement hybrid quantum systems. One such example is provided by a collection of nitrogen vacancies (NV) or color centers in diamond interacting with the magnetic field controlled by a superconducting resonator. This platform offers the advantage of large-N spins, actually implementing a good approximation of the thermodynamic limit since $N \approx 10^{12}$–10^{16} there, and physical conditions that allow to explore various regimes of both collective and local dissipation. The former is determined by the superconducting resonator quality factor, the latter by the intrinsic impurities of the condensed matter system and couplings to the crystal lattice. In these systems, superradiant light emission has been recently observed [108,110], as well as steady-state bistability and critical slowing down [111]. In the bad-cavity regime, the cavity mode decay allows an adiabatic elimination of the bosonic degree of freedom, allowing the implementation of effective spin Hamiltonians, while tuning spin subensembles in and out of resonance allows to vary N and thus study system-size scaling [108].

III. LIOUVILLIAN SPECTRUM AND PHASE TRANSITION

We begin our analysis by studying the spectral properties of the Liouvillian, which can signal the emergence of phase transitions [18]. We refer the interested reader to Appendix A and the referenced works for a more elaborate discussion.

Given any Liouvillian $\mathcal{L}$, we can introduce its eigenvalues λ_i and eigenmatrices $\hat{\rho}_i$, defined via the relation

$$\mathcal{L}\hat{\rho}_i = \lambda_i \hat{\rho}_i. \tag{5}$$

The steady state of the system under consideration is then given by the density matrix $\hat{\rho}_{ss}$ such that $\mathcal{L}\hat{\rho}_{ss} = 0$, i.e., the eigenmatrix of the Liouvillian associated to the zero eigenvalue. A fundamental role in the system dynamics is played by $\hat{\rho}_1$, that is the eigenmatrix associated to the smallest eigenvalue λ_1 bigger than zero, which describes the slowest relaxation scale toward the steady state. A phase transition takes place in the thermodynamic limit when λ_1 becomes exactly zero, both in its real and imaginary parts. For any finite size of the system under consideration, however, $\lambda_1 \neq 0$. Nevertheless, the study of λ_1 and $\hat{\rho}_1$ provides much useful information about the scaling and nature of the transition [41].

A. $\mathbb{PT}$ symmetry and Liouvillian antigap

There exists a class of non-Hermitian Hamiltonian systems which are invariant under the composition of unitary (parity $\mathcal{P}$) and antiunitary (time-reversal $\mathcal{T}$) transformations: the $\mathcal{PT}$ symmetry [112–114]. This $\mathcal{PT}$ symmetry cannot be directly extended to the Liouvillian case, due to the dissipative nature of the contractive dynamics [115]. However, certain systems admit a $\mathcal{PT}$-symmetric transformation once a shift parallel to an average damping rate is added to $\mathcal{L}$ [98]. Therefore, the $\mathbb{PT}$ symmetry of $\mathcal{L}$ is not a superoperator symmetry (that is, it does not describe a property of the steady state). Instead, it is a spectral property related to the emergence of a reflection symmetry of the eigenvalues in the complex plane, i.e., introducing a dihedral (D_2) symmetry. Indeed, there exist

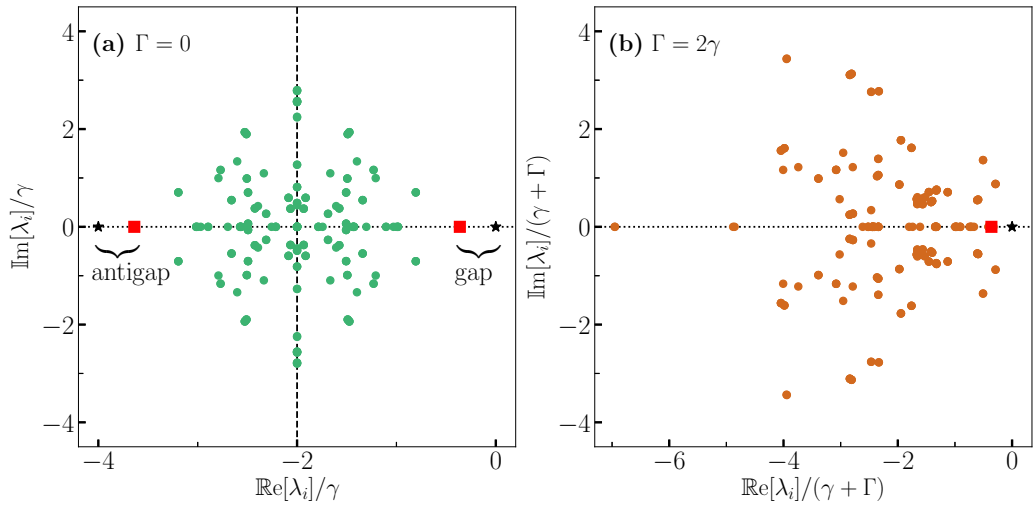

FIG. 2. Liouvillian spectrum for the dissipative *XYZ* model with local dissipation only $\Gamma = 0$ (a), and both local and collective dissipation $\Gamma = 2\gamma$ (b). Here, $N = 4$ and we choose $J_x/(\gamma + \Gamma) = 0.6$, $J_y/(\gamma + \Gamma) = J_z/(\gamma + \Gamma) = 1$. We mark λ_0 and λ_1 with a black star and a red square, respectively. All other eigenvalues λ_i are marked by circles. (a) The $\mathbb{PT}$ symmetry of the Liouvillian with only local dissipation is visible by the additional plane symmetry (vertical dashed line) of the eigenvalues (green circles). The Liouvillian gap and the Liouvillian *antigap* of the $\mathbb{PT}$-symmetric model are highlighted, showing the correspondence of λ_0 with λ_M (black star), and λ_1 with λ_{M-1} (red square). (b) The Liouvillian spectrum with local and collective dissipation, showing no $\mathbb{PT}$ symmtery.

a real number $\eta > 0$ such that, for all the eigenvalues λ_i, there exist a $\lambda_j = -2\eta + \lambda_i$. This can be easily visualized by plotting the eigenvalues of the Liouvillian in the complex plane $\lambda_j = x_j + i\, y_j$.

The $\mathbb{PT}$ symmetry results in a reflection symmetry of the eigenvalues with respect to a line $x = -\eta$ parallel to the imaginary axis [98,116,117]. The spectrum of the dissipative all-to-all connected *XYZ* spin model is shown in Fig. 2, setting $N = 4$, $J_x = 0.6J_z$, and $J_y = J_z$. In Fig. 2(a) we consider the case of homogeneous local dissipation, $\Gamma = 0$ in Eq. (2), and for comparison, the case of collective and local dissipation is shown in Fig. 2(b), $\Gamma = 2\gamma$ in Eq. (2), showing instead no additional symmetry in the spectrum. We have verified that the absence of $\mathbb{PT}$ symmetry occurs also in the case of collective dissipation only, $\gamma = 0$, $\Gamma \neq 0$. Similarly, also in the case of local dephasing and local pumping, the Liouvillian spectrum of the model displays the additional dihedral symmetry typical of $\mathbb{PT}$ symmetry.

To clarify the discussion, let us consider a $\mathbb{PT}$-symmetric Liouvillian with $(M + 1)$ eigenvalues. Therefore, there exists an eigenmatrix $\hat{\rho}_M$ whose eigenvalue is λ_M, which is the symmetric counterpart of $\hat{\rho}_{\rm ss}$. Since $\lambda_0 = 0$ and $\lambda_M = -2\eta$, we can directly access the value of η. Similarly, we can define the eigenmatrix $\hat{\rho}_{M-1}$ which mirrors $\hat{\rho}_1$, and an "antigap" λ_{M-1}, such that $\lambda_{M-1} - \lambda_M = \lambda_1$. This property allows for an easier numerical computation of the gap and associated $\hat{\rho}_1$. Indeed, if one is interested in computing only a few eigenvalues of the Liouvillian, one could resort to an iterative diagonalization method, based on Krylov subspaces. This method works extremely well for large-magnitude eigenvalues. However, if one is interested in computation of small eigenvalues, this method performs worse. Indeed, one has to invert the matrix $\mathcal{L}$, so that the eigenvalues of smallest magnitude become the most relevant ones. Moreover, for non-Hermitian matrices, this method is known to be unstable [118]. Knowing that the Liouvillian is $\mathbb{PT}$ symmetric (and knowing η) can mitigate these numerical problems: by considering the shifted Liouvillian $\mathcal{L}' = \mathcal{L} + 2\eta\, \mathbb{I}$, the steady state is characterized by $\lambda'_0 = 2\eta$ and $\lambda'_1 = 2\eta - \lambda_1$, where $\mathbb{I}$ is the identity matrix. Since $\lambda'_1 = -\lambda_{M-1}$, we will call the eigenmatrix obtained like that the $\mathbb{PT}$-symmetric antigap.

In a *XYZ* spin system, a sufficient condition to have this $\mathbb{PT}$-symmetric behavior is to have dissipation only on the border of the chain [116]. This condition is trivially satisfied for the all-to-all connected *XYZ* spin model with local dissipation since all spins are at the border of the system.

B. Closing of the Liouvillian gap: Critical slowing down

As detailed in Appendix A, the occurrence of a second-order phase transition in the *XYZ* model is marked by the closing of the Liouvillian gap in a whole region. In Fig. 3 we compute the Liouvillian gap exploiting the $\mathbb{PT}$-symmetric *antigap* method introduced in Sec. III A.

In Fig. 3(a), the real part of the Liouvillian gap, $\lambda = |{\rm Re}[\lambda_1]|$, is calculated as a function of J_y (normalizing both quantities by a fixed value of γ), for various system sizes N, also setting $J_z = \gamma$, $J_x = 0.6\gamma$. In Fig. 3(a), no critical behavior is observed for small or negative values of J_y/γ, hinting at the absence of an antiferromagnetic phase.

For positive J_y, the gap tends to close abruptly after $J_y/\gamma \simeq 1$. The minimum is for $J_y/\gamma \simeq 3$ for $N = 10$, and for larger values of J_y/γ we see that the Liouvillian gap again increases. However, by comparing $\lambda(N)$ for different system sizes, we see that for $J_y \gtrsim \gamma$, $\lambda(N) > \lambda(N + 1)$. This aspect corroborates the idea that a second-order dissipative phase transition is occurring, as these are characterized by a closing of the gap over an extended region of the control parameter [18].

In Fig. 3(b), we plot the minimum of the Liouvillian gap for each system size N of Fig. 3(a) against the system size

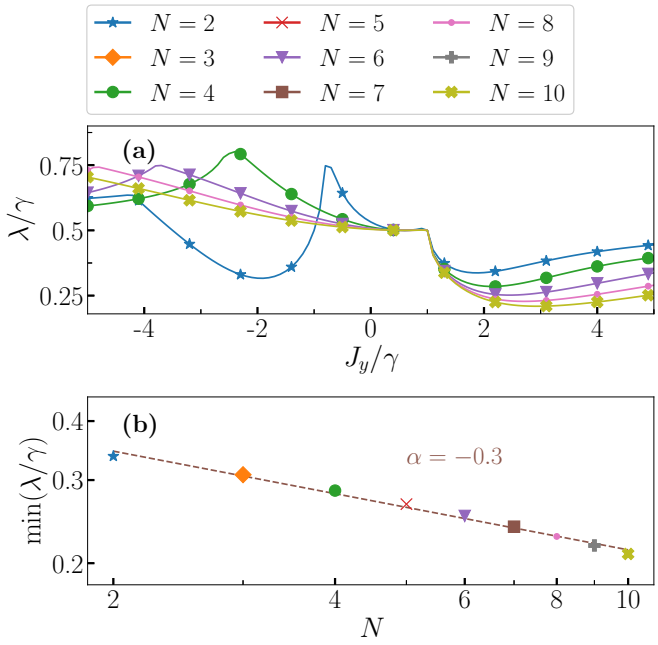

FIG. 3. Study of the Liouvillian gap, in units of the local dissipation rate γ, and its critical slowing down for the dissipative *XYZ* model with local dissipation only. The system parameters are chosen as specified in Fig. 4(b). (a) The Liouvillian gap λ is plotted as a function of J_y/γ for various system sizes $N = 2, \ldots, 10$. The markers are only a guide for the eye (101 points have been calculated for each value of N). (b) The minimum of the Liouvillian gap, normalized by γ, for each of the curves in the top panel is plotted as a function of the system size N in a log-log plot, showing a linear scaling of the Liouvillian gap typical of phase transition [$\min(\lambda) \propto N^{\alpha}$, with exponent $\alpha = -0.3$] leading to a critical slowing down in the thermodynamic limit.

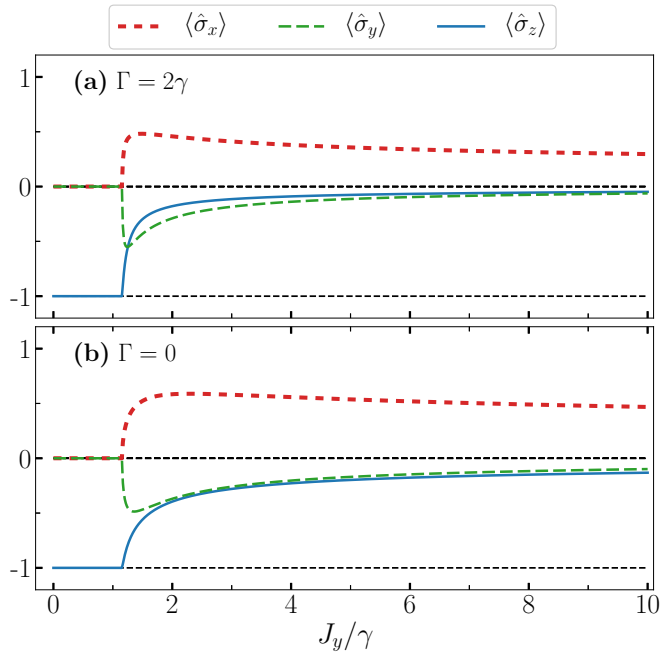

FIG. 4. Steady-state solution of the mean-field equations (6) in the case $\Gamma = 2\gamma$ (a) and in the case $\Gamma = 0$ (b), having fixed the value $(\gamma + \Gamma) = 1$. The parameters used here are $J_x/(\gamma + \Gamma) = 0.6$, $J_z/(\gamma + \Gamma) = 1$, and $N \to \infty$. The horizontal black dashed lines correspond to $\langle \hat{\sigma}_\alpha \rangle = 0, -1$.

in a log-log plot. Since the position of the minimum changes for each system size, the minimum of the Liouvillian gap allows us to estimate the slowest timescale of the system. The shift of the minimum is due to finite-size effects; we refer the interested reader to Appendix B for a more in-depth discussion of these finite-size effects and the finite-size scaling. Given the excellent fit by a power law $\min(\lambda/\gamma) = \beta N^{\alpha}$ with exponent $\alpha = -0.3$, we conclude that for $N \to \infty$ there is a diverging timescale (i.e., a critical slowing down) associated to $\gamma/\min(\lambda)$, resulting in the presence of multiple steady states.

Having demonstrated via spectral analysis the presence of the paramagnetic-to-ferromagnetic phase transition and the absence of an antiferromagnetic regime, we focus now the properties of the steady-state density matrix, obtained both via Gutzwiller MF analysis and via exact numerical resolution of the equation of motion.

IV. MEAN-FIELD PHASE DIAGRAM

One can derive the mean-field equations for the system by calculating the time dependence of the expectation values of the Pauli matrices and assuming a Gutzwiller ansatz for the density matrix. In other words, we calculate $\mathrm{Tr}[\partial_t \hat{\rho}(t) \hat{\sigma}_i^{\alpha}]$, with $\alpha = x, y, z$, the time dependence of the magnetization in each direction. The Gutzwiller ansatz for the system density matrix amounts to assuming that $\hat{\rho}(t)$ is the tensor product of identical density matrices, each one representing the state of the jth spin, $j = 1, \ldots, N$. Under this hypothesis, the Lindblad master equation (2) can be recast as

$$\partial_t \langle \hat{\sigma}^x \rangle = 2(J_y - J_z) \langle \hat{\sigma}^y \rangle \langle \hat{\sigma}^z \rangle - \frac{\tilde{\gamma}}{2} \langle \hat{\sigma}^x \rangle + \frac{\Gamma}{2} \langle \hat{\sigma}^x \rangle \langle \hat{\sigma}^z \rangle, \tag{6a}$$

$$\partial_t \langle \hat{\sigma}^y \rangle = 2(J_z - J_x) \langle \hat{\sigma}^x \rangle \langle \hat{\sigma}^z \rangle - \frac{\tilde{\gamma}}{2} \langle \hat{\sigma}^y \rangle + \frac{\Gamma}{2} \langle \hat{\sigma}^y \rangle \langle \hat{\sigma}^z \rangle, \tag{6b}$$

$$\partial_t \langle \hat{\sigma}^z \rangle = 2(J_x - J_y) \langle \hat{\sigma}^x \rangle \langle \hat{\sigma}^y \rangle - \tilde{\gamma}(\langle \hat{\sigma}^z \rangle + 1) - \frac{\Gamma}{2}\left(\langle \hat{\sigma}^x \rangle^2 + \langle \hat{\sigma}^y \rangle^2\right), \tag{6c}$$

having defined $\tilde{\gamma} = \gamma + \Gamma/(N-1)$ and $\langle \hat{\sigma}^{\alpha} \rangle$ the single-site approximation of the Pauli matrix expectation values, with $\alpha = x, y, z$.

Equation (6) cannot be analytically solved, even in the steady state ($\partial_t \langle \hat{\sigma}^{\alpha} \rangle = 0$). Indeed, the inclusion of collective emission introduces nonlinear terms that, for Eqs. (6a) and (6b), are similar to the Hamiltonian ones, hinting at the fact that they contribute to entanglement generation in the dynamics. Similarly, the presence of local dissipation prevents the equation of motion from being simplified since the spin length, Eq. (C1), is not preserved. Both the local and collective dissipation, however, act as an effective transverse magnetic field in the z direction.

We plot the MF solution to Eq. (6) in Fig. 4 in the case $\Gamma = 2\gamma$ [Fig. 4(a)] and in the case $\Gamma = 0$ [Fig. 4(b)]. The

total dissipation ($\gamma + \Gamma$) is kept fixed. We notice that both MF solutions predict a second-order phase transition and that the value of J_y triggering the phase transition is the same in both cases. However, the two plots exhibit a different dependence of the mean values $\langle \hat{\sigma}^\alpha \rangle$ on J_y, with $\alpha = x, y, z$. In the presence of local and collective dissipation [Fig. 4(a)], the transition appears to be sharper than in the presence of local dissipation only [Fig. 4(b)].

Local dissipation only

Here, we briefly analyze the case $\Gamma = 0$ in Eq. (6), which was extensively investigated in Refs. [25,27,38,52,55,87–89,119] in lower dimensions and in Ref. [49] in infinite dimension. We notice that, in this case, Eqs. (6) only contain nonlinear *homogeneous* terms, and one can thus obtain $\langle \hat{\sigma}^\alpha \rangle_{\rm ss}$ exactly. A discussion of the properties of this model in presence of only collective dissipation can be found in Appendix C.

We study the mean-field phase diagram through an instability analysis analogous to the one performed for the nearest-neighbor *XYZ* Hamiltonian [25]. We determine the instability of the paramagnetic phase in the xy plane to a d-dimensional perturbation with wave vector $\vec{k}$. To this end, a Fourier transform of (6) is performed in which the perturbations can be easily applied. Due to the all-to-all connected structure, the perturbations with wave vector $\vec{k} = (k_1, k_2, \ldots, k_d)$ are restricted by k_l only being able to attain the values 0 and π. A straightforward calculation shows that the presence of an antiferromagnetic phase ($k_l = \pi$) is nonphysical for any value of the coupling parameters. Hence, the mean-field phase diagram consists only of a paramagnetic phase and a ferromagnetic one ($k_l = 0$). The latter is present when the condition

$$-\frac{\gamma^2}{16} > (J_x - J_z)(J_y - J_z) \tag{7}$$

is fulfilled, which is found by applying the perturbations with $k_l = 0$. In the following, we will choose $J_x/\gamma = 0.6$ and $J_z/\gamma = 1$. Consequently, we can define the critical y coupling $J_y^{\rm c}$ as the minimal J_y satisfying Eq. (7), i.e.,

$$\frac{J_y^{\rm c}}{\gamma} = \frac{J_z}{\gamma} + \frac{\gamma}{16(J_z - J_x)} = 1.15625. \tag{8}$$

The absence of an antiferromagnetic phase in this all-to-all connected model can be expected. Each spin is connected to every other spin in the system, and no unique spatial structure is present for this type of interaction. It is impossible for the spins to take alternating directions with respect to their neighbors. The results of this instability analysis lead to the phase diagram shown in Fig. 5, where the black dashed-dotted curves show the transition boundary between both phases according to the mean-field approximation.

Having derived the MF solutions and the phase diagram, we will now proceed to study the dynamics in the full quantum formalism, beyond results found for dissipative spin-boson models [20,120]. Since we show that, at the MF level, the model with local and collective dissipation displays a second-order phase transition similar to the local dissipation only case, we will at first focus on the latter case.

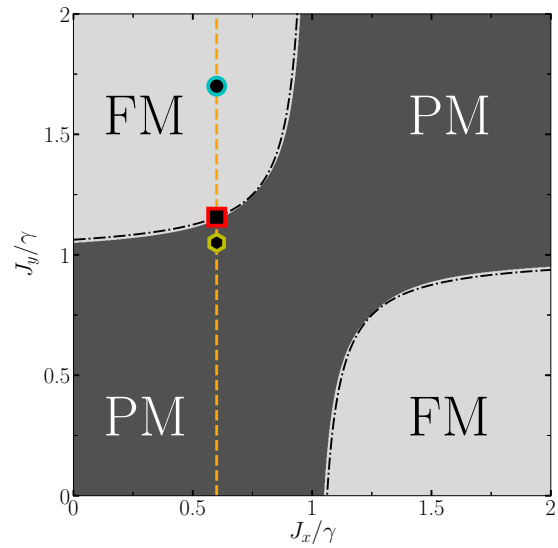

FIG. 5. Phase diagram for local dissipation only, where $\Gamma = 0$ and $J_z/\gamma = 1$. The phases are determined from the intersection in the bimodality coefficient curves for in the x and y directions for $N = 50$ and 60, i.e., the transition from a paramagnetic phase (PM) to a ferromagnetic phase (FM) in the xy plane. The black dashed-dotted curves show where the transition takes place in the mean-field approximation, while the background color defines the PM (dark gray) and FM (light gray) regions from calculations using the bimodality coefficient in the full quantum model (discussed in Sec. V B). The orange vertical dashed line is located at $J_x = 0.6\gamma$ and shows the cut that will be used in the next figures to characterize the phase transition. The three points on the cut $J_x/\gamma = 0.6$ indicate the values of J_y/γ which will be used for benchmarking the MF with the full quantum solutions: $J_y/\gamma = 1.1$, in the PM phase (hexagon with yellow contour), at criticality, $J_y/\gamma = 1.15625$ (square with red contour), and at $J_y/\gamma = 1.7$ in the moderately anisotropic FM region (circle with a cyan contour).

V. MEAN-FIELD VALIDITY ACROSS THE PHASE DIAGRAM

To compare the mean-field analysis to the full quantum solution, we interpret the all-to-all coupled spin system as a d-dimensional system. Every time we add a spin, the dimension of the system is also increased by one. This implies that a d-dimensional system consists of d spins and that infinite dimensions are reached when the system has an infinite amount of spins. Hence, we test if mean-field theory becomes exact in infinite dimensions, i.e., for an infinite number of spins.

In the following, we use the permutational invariant quantum solver (PIQS) [92], a module of QUTIP, the quantum toolbox in Python [121,122], developed to efficiently solve problems with permutational invariance (see also Appendix D). This is an open-source computational library that leverages the flexibility of numerical and scientific Python libraries (NUMPY and SCIPY) and implements efficient numerical techniques by interfacing with the Intel Math Kernel Library (MKL). Performance is enhanced by using compiled scripts in Cython and by natively supporting cross-platform parallelization on clusters, with open multi-processing (Open MP) [121,122]. To obtain the steady-state density matrix, we will

use the `direct` method of the `qutip.steadystate` solver, which is based on the lower-upper (LU) decomposition of the Liouvillian matrix to solve the equation $\mathcal{L}\hat{\rho}_{\rm ss} = 0$. The results are exact up to numerical tolerance (having set the absolute tolerance to 10^{-12}).[1] We will characterize criticality by calculating the expectation values of operators on the steady-state density matrix of the system, i.e., $\langle \hat{A} \rangle_{\rm ss} = {\rm Tr}[\hat{A}\hat{\rho}_{\rm ss}]$, and by investigating the properties of $\hat{\rho}_{\rm ss}$ (see Appendix D for details).

Based on the preliminary study of the MF solution and of the Liouvillian gap (see Figs. 3 and 5), and Secs. IV and III B, we can identify three main regions in the phase diagram of the *XYZ* model: (i) paramagnetic far from criticality ($J_y \leqslant J_x$); (ii) critical ($J_x < J_y \leqslant J_y^{\rm h}$); (iii) highly anisotropical ($J_y > 2.3\gamma = J_y^{\rm h}$) (see discussion in Sec. V C). The paramagnetic one (i) seems to present a saturation of the Liouvillian gap and no antiferromagnetic phase for $J_y \leqslant 0$. We may argue that this region can be safely approximated by a MF solution. We numerically tested this hypothesis, and found it to be correct (not shown).

In the critical region (ii), a fundamental question is the determination of both the existence and the position of the critical point. Regardless of our ability to determine the point of transition, we are able to access the validity of the mean-field solutions through a finite-size scaling. For almost-critical anisotropy, we will consider three domains: (1) the paramagnetic region before the transition $J_x < J_y < J_y^{\rm c}$; (2) the critical point according to MF prediction $J_y = J_y^{\rm c}$; (3) the ferromagnetic region $J_y^{\rm c} < J_y < J_y^{\rm h}$. These are, respectively, represented as the yellow hexagon, the red square, and the blue circle in the phase diagram of Fig. 5.

Finally, we are interested in the properties of the high-anisotropy phase (iii). The MF does not predict a second phase transition to a paramagnetic phase. Nevertheless, several different methods [25,27] have pointed out that this regime of parameters leads to a completely different behavior with respect to the standard ferromagnetic phase.

Note that in all the curves in this section which show the behavior of the system as a function of J_y/γ, the markers on the curves are a guide for the eye, and each curve is obtained from a simulation of 100 points. We also computed more values of the system size N than those shown in those figures.

In the following we choose, unless specified otherwise, $J_z = \gamma$, $J_x = 0.6\gamma$ and we vary J_y.

A. Critical region

To characterize the properties of the steady state, we consider the spin-structure factor in the x direction

$$S^{xx}(N) = \frac{1}{N(N-1)} \sum_{j \neq l} \left\langle \hat{\sigma}_j^x \hat{\sigma}_l^x \right\rangle_{\rm ss}, \tag{9}$$

the z magnetization

$$M_z = \langle \hat{S}^z \rangle_{\rm ss}/N = {\rm Tr}[\hat{S}^z \hat{\rho}_{\rm ss}]/N, \tag{10}$$

and the von Neumann entropy

$$S = S[\hat{\rho}_{\rm ss}] = -\sum_i p_i \ln(p_i), \tag{11}$$

where p_i are the eigenvalues of the density matrix $\hat{\rho}_{\rm ss}$. While at MF level it is possible to have $\langle \hat{\sigma}^x \rangle \neq 0$, for any finite-size system the $\mathcal{Z}_2$ symmetry imposes $\langle \hat{\sigma}^x \rangle = 0$ (see the discussion in Appendix A). The spin-structure factor $S^{xx}(N)$ contains information on the orientation of the spins with respect to each other and can be different from zero even for finite-size systems. Ferromagnetic order is present in the xy plane if the steady-state spin-structure factor in the x direction or (and) the y direction is different from zero. The magnetization M_z, instead, is expected to show a first-order discontinuity, according to the mean-field prediction. Finally, we will use the von Neumann entropy per spin $S(N)/N$, it is an indicator of the degree of mixture of the steady state. A detailed discussion of these observables can be found in Appendix E.

In Fig. 6 we plot the spin-structure factor [Fig. 6(a)], the z magnetization [Fig. 6(b)], and the von Neumann entropy [Fig. 6(c)] in the region $0.75 < J_y/\gamma < 1.75$ for different values of N, and we compare them to the results obtained via MF analysis (black dashed curve) of which the calculation is explained in Appendix D. Note that we define the point where the mean field predicts a change between the PM and FM phases as the critical point. All the three top panels of Fig. 6 show that the results of the full quantum simulations become closer to the MF prediction by increasing the number of sites. Nevertheless, we notice that the results at the critical point are still in visible disagreement with respect to those obtained via MF analysis.

We thus identify a paramagnetic and a ferromagnetic phase in qualitative agreement with the mean-field calculations. Note that, as a result of finite-size effects, the transition from the paramagnet to the ferromagnet is smoothed, making it difficult to pinpoint the exact location of the phase transition, even more so as the region close to the transition is subject to sizable fluctuations. We will return to the determination of the point of transition in Sec. V B.

Normally, one expects the finite-size effects to disappear in the thermodynamic limit. To better quantify whether the exact quantum solutions would retrieve the mean-field results for $N \to \infty$, we study the absolute difference between the full quantum solution and the MF prediction for corresponding N,

$$\Delta S^{xx}(N) = \left| S^{xx}(N) - S^{xx}_{\rm MF}(N) \right|, \tag{12a}$$

$$\Delta M_z(N) = |M_z(N) - M_{z\,{\rm MF}}(N)|, \tag{12b}$$

$$\Delta S(N) = |S(N) - S_{\rm MF}(N)|, \tag{12c}$$

for the steady-state spin-structure factor, the z magnetization, and the von Neumann entropy, respectively. How these quantities fare as a function of J_y is shown in Figs. 6(d)–6(f). The discrepancies are largest at the critical point (marked by a vertical red dashed line in each panel) and in general the MF tends to perform better in the anisotropic FM region $J_y > J_z, J_x$ than in the PM region. We will better investigate the highly anisotropic region in Sec. V C. As a general trend,

[1]The interested reader can find a series of notebooks dealing with similar systems in the section "Permutational invariant Lindblad dynamics" of the QUTIP project tutorials http://qutip.org/tutorials.

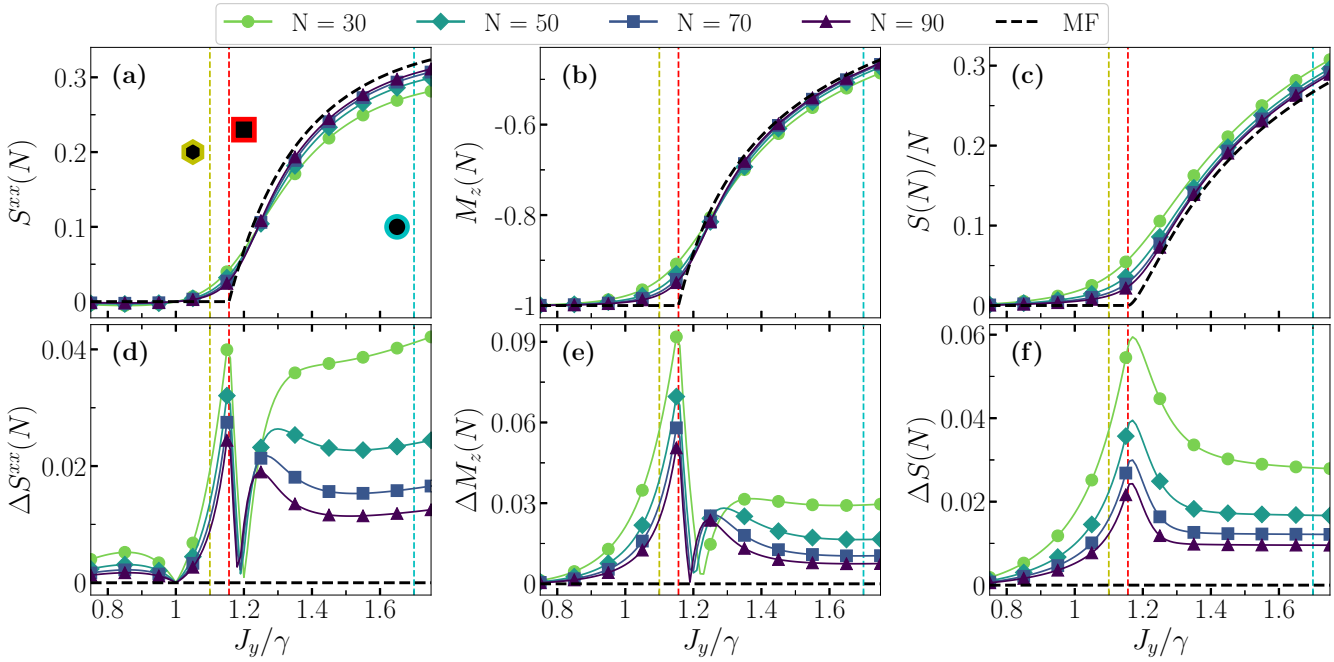

FIG. 6. Study of the paramagnetic-to-ferromagnetic dissipative phase transition in the presence of only local dissipation for the system parameters specified in Fig. 4(b). The first row shows the steady-state spin-structure factor in the x direction (a), the z magnetization (b), and the von Neumann entropy per spin (c) as a function of J_y for different system sizes (N increases for darker curves). The markers are a guide for the eye, 100 points are calculated for each curve. The second row shows the absolute value of the difference between the variables in the corresponding upper panel and the mean-field value for $N \to \infty$. (d) $\Delta S^{xx}(N) = [S^{xx}(N) - S^{xx}_{\rm MF}(N)]/N$. (e) $\Delta M_z(N) = [M_z(N) - M_{z\,\rm MF}(N)]/N$. (f) $\Delta S(N) = [S(N) - S_{\rm MF}(N)]/N$. See Eq. (12) for details. In all panels, the black dashed curve represents the MF value. The dashed vertical lines refer to the points chosen in Fig. 5 and also studied for the system-size scaling in Fig. 7: the PM phase (yellow line, hexagon marker); the critical point (red line, square marker); the FM phase (cyan line, circle marker).

we can see that, as the system size is increased, the difference between the MF and the computed quantities from the quantum $\hat{\rho}_{\rm ss}$ becomes smaller. However, the three curves display different behaviors in their scaling properties.

In Fig. 7 we show the finite-size scaling of the solution toward the MF, for the quantities of Eq. (12), for the following three regions: (i) paramagnetic, $J_y/\gamma = 1.1$ [Fig. 7(a)]; (ii) critical, $J_y/\gamma = J_{y,c}/\gamma$ [Fig. 7(b)]; (iii) ferromagnetic, $J_y/\gamma = 1.7$ [Fig. 7(c)]. We notice that all the results display a power-law behavior up to good approximation. Thus, we perform a power-law fit of the form $y = \beta N^{\alpha_i}$ for unknown coefficients β and α_i. Clearly, α_i are negative for each observable, i.e., the mean-field solutions are in fact exact in the thermodynamic limit. However, different quantities in different regimes present different behaviors. We notice that the ferromagnetic phase presents the highest convergence rate, the critical region being the slowest-converging one. This is surprising since even if the critical point is at lower entropy than the ferromagnetic region, the latter can be better captured by a Gutzwiller ansatz. Indeed, the ferromagnetic structure is not that of an ordered phase in which all the spin tends to be aligned, but every spin is, instead, in the same mixed state. Instead, at criticality, the system shows significant fluctuations around the MF results, which slows the convergence rate regardless of the less mixed nature of the system.

B. Pinpointing the phase transition: Success of the bimodality coefficient and failure of the averaged susceptibility

Having proved that the MF results recover the expected outcomes in the thermodynamic limit, we turn our attention now to the study of the critical point in finite-size systems. Indeed, in any experiment, one cannot access an infinite number of spins, but instead one has to infer the presence of criticality via finite-size scaling. In this regard, we consider which quantity can better infer the existence of a phase transition in the thermodynamic limit.

In Fig. 8(a) we show results for $J_x = 0.6\gamma$. The vertical black dashed-dotted line shows the mean-field prediction for the position of the phase transition, the vertical red dashed line shows the position as predicted by the point of intersection of the bimodality coefficient $B_c = \langle(\hat{S}^x)^2\rangle^2_{\rm ss}/\langle(\hat{S}^x)^4\rangle_{\rm ss}$ between the curves $N = 50$ and 60. It is clear that finite-size effects impose a quantitative difference with the mean-field prediction for the location of the phase transition. Comparing the results for finite-size systems to those of the MF (Fig. 5), the qualitative behavior is, however, in good agreement. Moreover, the phases on either side of the transition coincide. On the left we see the values of the bimodality coefficient approaching $\frac{1}{3}$, indicating a unimodal, i.e., paramagnetic, region. And, on the right side, they approach 1, indicating a bimodal region, i.e., a ferromagnetic one.

One can wonder if there actually is a quantitative agreement in the thermodynamic limit and, if not, how large the

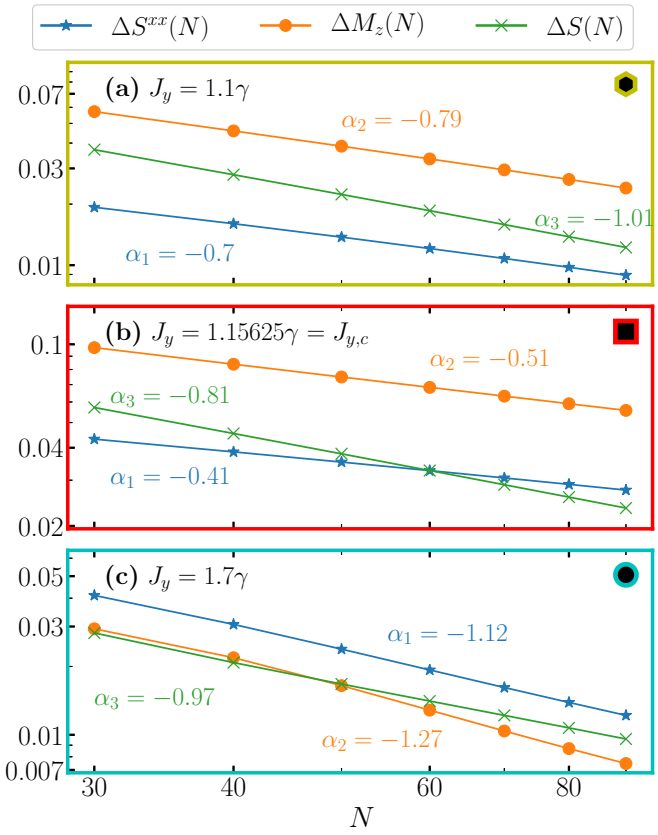

FIG. 7. The panels show the finite-size scalings of the quantities plotted in Fig. 6 for $J_y/\gamma = 1.1$ (a), $J_y/\gamma = J_{y,c}/\gamma$ (b), and $J_y/\gamma = 1.7$ (c). We show the exponents α of a power-law fit of the form $y = \beta N^{\alpha_i}$ next to the curves, for unknown coefficients β and α_i. The absolute difference of the spin-structure factor with respect to the MF prediction, for corresponding value of N, is marked by a blue line with stars and fit by α_1. Similarly, in each panel the z-magnetization MF discrepancy is marked by an orange line with circles and exponent α_2, while the von Neumann entropy is marked by a green line with crosses, the exponent for the fit given α_3. The markers in the top-right corner of each panel refer to the points in the phase diagram of Fig. 5.

quantitative deviation from the mean-field value is. To gain a better idea of this, we show the point of transition as predicted by the point of crossing of the bimodality coefficient curves for N and $(N+5)$ as a function of $1/N$ in Fig. 8(b). As the system size increases, the point of transition moves toward the mean-field critical point. Even though we can simulate systems with a number of spins of the order of 100, we are still far away from the thermodynamic limit. To gain an estimate of the convergence in the thermodynamic limit, we make a polynomial fit of third (orange dashed line) and fourth degree (green dashed-dotted line). These results show us that in the thermodynamic limit, the critical point is predicted with a reasonable, although not excellent, accuracy.

In Figs. 8(c) and 8(d) we report on a study of the angular-averaged susceptibility χ_{av}, as introduced in Ref. [52] (see Appendix E for a definition). We find that this quantity *is not a good predictor* of the position of the phase transition for finite number of spins N in the all-to-all connected XYZ spin model with local dissipation. Even if for small-N values the maximum of the susceptibility keeps shifting toward bigger J_y/γ as N increases, for bigger N the peak is at a value $J_y \simeq 1.35\gamma$ [Fig. 8(c)]. This value is different from that of the transition point predicted by the MF. However, χ_{av} becomes divergent for $N \to \infty$, as shown in Fig. 8(d). A log-log fit of the maximum extracts an exponent $\alpha = 1.1$. We conclude that the angular-averaged susceptibility, while signaling a divergence, is not associated to the one of the symmetry breaking. This is in stark contrast with lower-dimensional cases [52].

C. Highly anisotropic regime: Highly entropic ferromagnet

We now focus on the study of the high-anisotropy regime. We define it as the region of J_y/γ where the phase is ferromagnetic but S^{xx} decreases. In our case, this corresponds to $J_y > 2.3\gamma$. We verified that this point coincides exactly to that where the bimodality coefficient obtained via the MF solution starts to decrease. In this regard, the high-anisotropy regime is the one where, by increasing J_y, the ferromagnetic phase peaks become less distinguished.

As already stated, this regime is particularly interesting. Indeed, far from isotropy, the simultaneous creation of two spin excitations is energetically favorable. The Hamiltonian part tends to create correlations in the lattice while dissipation can act continuously to destroy them. The competition between the two actions creates very mixed and correlated states. Indeed, the state remains very entropic even in the limit in which the Hamiltonian should dominate the dynamics.

Figure 9 shows a detailed study of the steady-state spin-structure factor in the x direction. We recall that in Fig. 6 we found that, for low anisotropy (i.e., $|J_x - J_y|$ small), the exact results converged quite well to the mean-field calculations, for the steady-state spin-structure factor as well as for the other quantities. For large anisotropy, this appears no longer true, as illustrated by Fig. 9(a) up to $J_y/\gamma = 30$. In Fig. 9(b) we highlight the difference to the mean-field prediction, Eq. (12). A study on the scaling of the exponent $S^{xx}(N) \propto N^{\alpha_1}$ is given in Fig. 9(c), for each point J_y/γ, up to $J_y/\gamma = 100$, extracting the exponent for different values of N. Even though the scaling predicts a very slow convergence to the mean field (e.g., $N^{-0.22}$ for $J_y/\gamma > 60$) we derive a very different description of this regime. Since these exponents tend to zero for larger J_y coupling, the MF prediction becomes less and less accurate the more we enter in the anisotropic regime. The inset in Fig. 9(c) provides a log-log scale of $|\alpha_1|$ versus J_y/γ to even better illustrate the presence of different scaling regimes. The plots of Figs. 6 and 9 show that the correctness of the mean-field solutions depends on the parameter regime. More specifically: for low anisotropy it holds, and for larger anisotropy it does not.

We conclude that, even if there is not a second phase transition, in actual realization of the model the high-anisotropy regime can be seen as profoundly different from the low-anisotropy ferromagnet. Not only does the order parameter in the MF become smaller and smaller, but the convergence of the full quantum solution toward the MF also becomes slower and slower. In this regard, the high-anisotropy region of the phase diagram seems to be inaccessible via experimental studies.

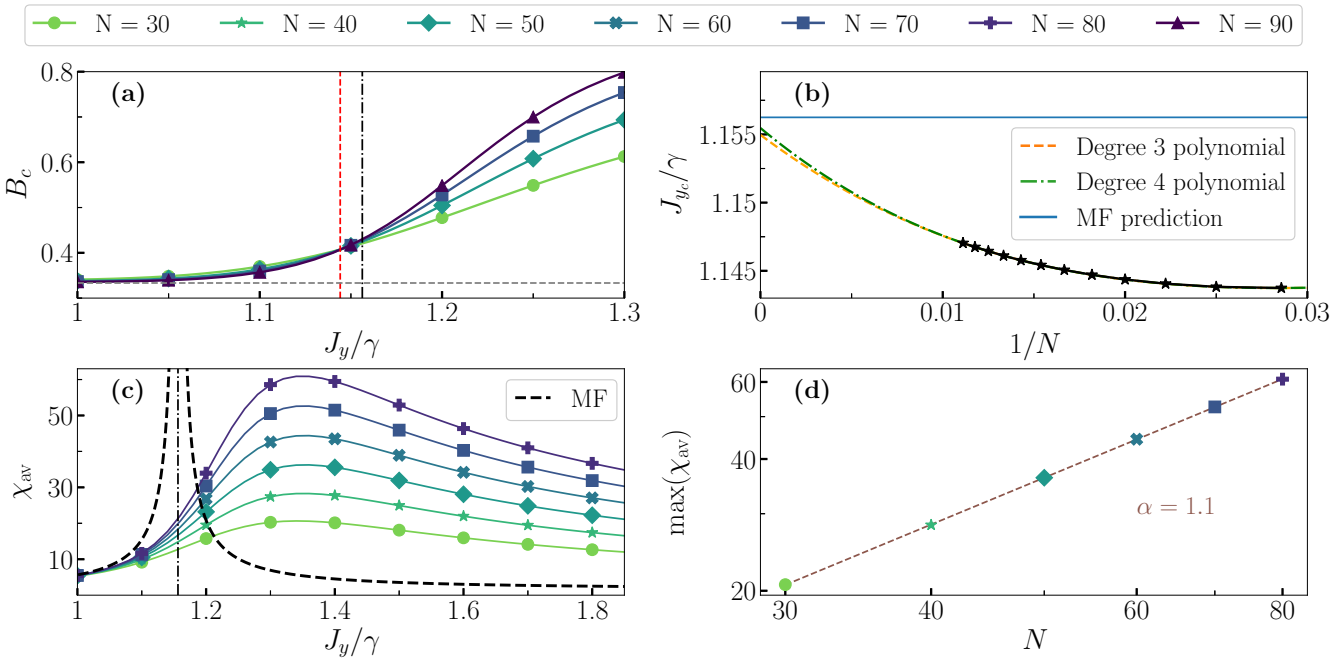

FIG. 8. Study of the location of the phase transition using bimodality coefficient (upper row) and the angular-averaged susceptibility (lower row) for the system parameters specified in Fig. 4(b). (a) Bimodality coefficient in the x direction, where the critical point in the mean field (black dashed-dotted line) is $J_{y,mf} = 1.15625\gamma$ and in the exact solution (red dashed line) $J_{y,e} = 1.144\gamma$, as determined by the intersection of the $N = 50$ and 60 curves. The (gray) horizontal dashed line indicates the value $\frac{1}{3}$, expected for the PM phase. (b) Point of transition as predicted by the intersection of the bimodality coefficient for systems with N and $(N + 5)$ spins (black full line with stars). The (blue) horizontal line indicates the mean-field prediction and the (orange) dashed and (green) dashed-dotted curves, respectively, show a polynomial fit of degree three and four. The lower panels show a study of the angular-averaged susceptibility for increasing system size N. (c) The angular-averaged susceptibility χ_{av} is studied as a function of J_y. The black dashed-dotted line shows the mean-field critical point. (d) Scaling of the maximum of the angular-averaged susceptibility as a function of the systems size N. The log-log fit extracts an exponent $\alpha = 1.1$.

D. Benchmark in the presence of local and collective dissipation

Finally, we consider the most general case in Eq. (2), for $\gamma \neq 0$ and also $\Gamma \neq 0$, i.e., we study the interplay of local and collective dissipation. The results of our numerical investigations are summarized in Figs. 10 and 11. The main observations are that the nature and position of the phase transition are not modified by the inclusion of collective dissipation, while some more refined qualitative features are affected, as also predicted by the MF solutions.

Notably, the phase transition seems to become sharper, as highlighted both by the magnetization and spin-structure

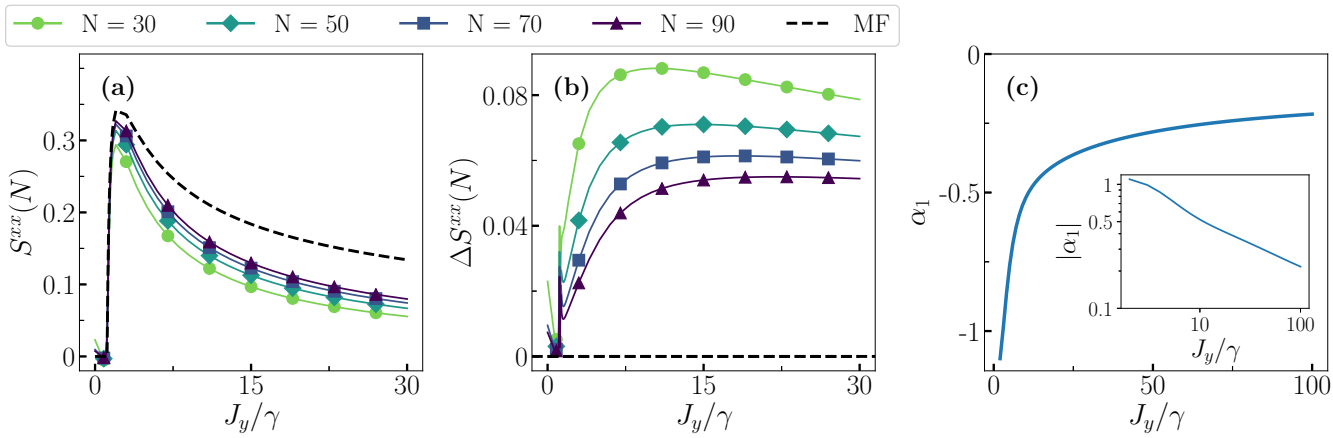

FIG. 9. Study of the highly anisotropic ferromagnet and of the mean-field approximation validity, for local dissipation only. We set the system parameters as specified in Fig. 4(b) and study the spin-structure factor as a function of J_y for different system sizes (lighter to darker curves as N increases). (a) Spin-structure factor $S^{xx}(N)$, calculated from the steady-state density matrix obtained from the Liouvillian in a fully quantum picture. (b) Absolute difference between $S^{xx}(N)$ and the MF approximation for corresponding N. (c) A power-law fit of the form $y = \beta N^{\alpha_1}$ is performed for $S^{xx}(N)$ for various points of J_y, using all the curves for different N in (a), but up to the value $J_y/\gamma = 100$. The inset highlights the variations in scaling with a log-log plot of $|\alpha_1|$.

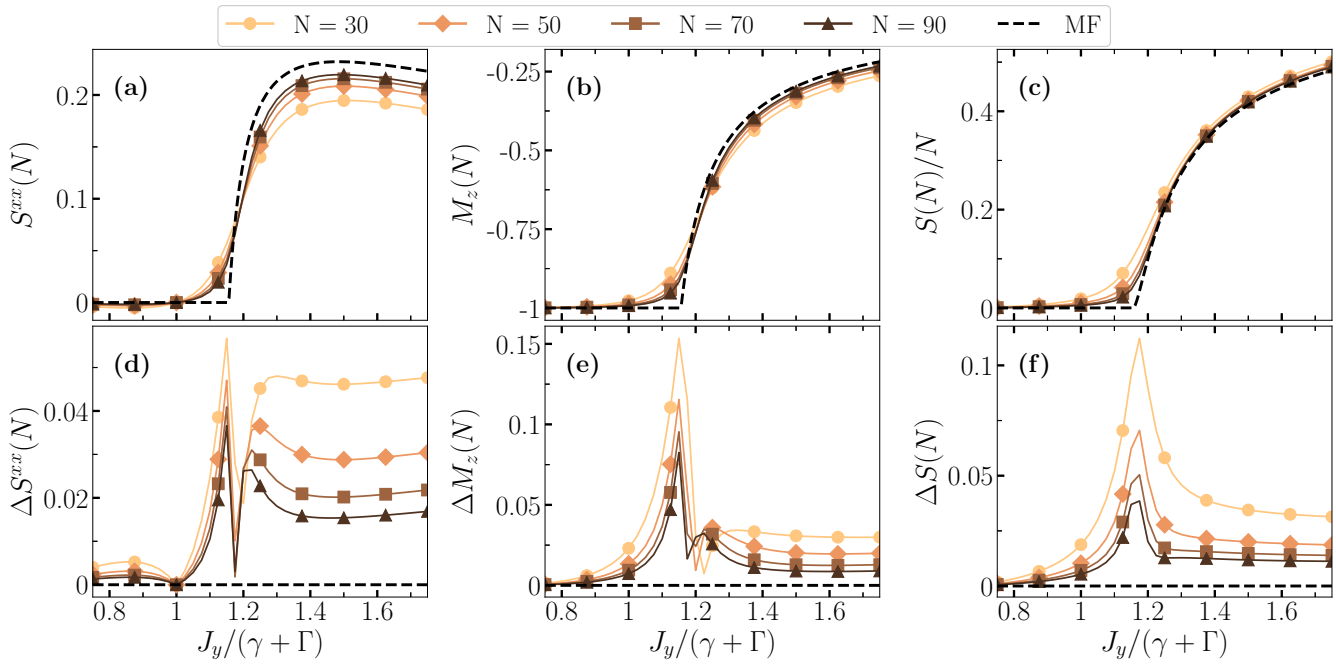

FIG. 10. Study of the system in the presence of both local and collective dissipation near the paramagnetic-to-ferromagnetic dissipative phase transition for the system parameters specified in Fig. 4(a). The plots show the same quantities and parameter range for $J_y/(\gamma+\Gamma)$ as Fig. 6 (there $\Gamma = 0$). (a) Spin-structure factor $S^{xx}(N)$. (b) z magnetization $M_z(N)$. (c) von Neumann entropy per spin $S(N)/N$. In all upper panels, the black dashed curve represents the MF value for $N \to \infty$. The lower panels highlight the discrepancy with the mean field for fixed N [see Eq. (12)]. (d) $\Delta S^{xx}(N) = [S^{xx}(N) - S^{xx}_{\rm MF}(N)]/N$. (e) $\Delta M_z(N) = [M_z(N) - M_{z\,\rm MF}(N)]/N$. (f) $\Delta S(N) = [S(N) - S_{\rm MF}(N)]/N$.

behavior as a function of J_y across the critical region, in Figs. 10(a) and 10(b). Similar features where observed when studying the Lipkin-Meshkov-Glick model with local and collective dissipation [49]. The von Neumann entropy, shown in Fig. 10(c), displays an excellent agreement with the MF prediction as the system size increases. Note that, similarly to Fig. 6, the markers on the curves provide a guide for the eye, and 100 points are calculated for each curve as a function of J_y. In the lower row of Figs. 10(d)–10(f), we more precisely measure the difference from the MF result, showing that the highest discrepancies occur at the point of the phase transition and as the J_y/γ normalized anisotropic coupling is increased.

Moreover, in Fig. 11 we report the scaling of these quantities, as a function of N, in the PM region [Fig. 11(a)], at criticality [Fig. 11(b)], and in the FM region with moderate anisotropy with respect to the $|J_y - J_x|$ ratio [Fig. 11(c)]. Interestingly, Fig. 11(b) shows that, at criticality, the same exponents as for the local dissipation case (see Fig. 7) for α_2 (z magnetization) and α_3 (von Neumann entropy per spin) are expected, with a slight discrepancy for α_1 (spin-structure factor). Similarly to the local-dissipation-only dynamics, in the FM anisotropic region, shown in Fig. 11(c), the system is well described by the MF even for low number of spins, as highlighted by $\Delta M_z(N)$, which decreases faster than a power-law behavior. Indeed, the magnetization absolute difference with respect to the MF displays a remarkable nonlinear trend, that does not seem well captured by a linear fit in a log-log plot (a fit would produce $\alpha_2 = -1.14$, shown as a dashed orange curve). This highlights the competition of processes governed by different scaling laws, hinting at the competition between local and collective dissipation even for remarkably large system sizes, $N \approx 100$.

VI. CONCLUSIONS

In full generality, the analysis performed in this paper provides a benchmark for spin models on the correctness of mean-field theory in dissipative systems. We studied the steady-state properties of an all-to-all connected dissipative spin model and tested the validity of the Gutzwiller mean-field approximation in capturing them.

Specifically, we considered the benchmark model of the *XYZ* anisotropic Heisenberg spin system, subject to both local and local-and-collective dissipation in the Lindblad form. This model is particularly interesting because it shows a second-order phase transition from a paramagnetic to a ferromagnetic phase. Moreover, for large anisotropy, this model presents a highly entropic regime which was debated to be a different phase according to cluster mean-field computations [27].

We simulated systems up to $N = 95$ spins exploiting the permutational symmetry of the model [92]. We demonstrate that, in both cases, the mean field correctly captures the physics in the thermodynamic limit. However, the scaling in the low-anisotropy regime strongly differs from that in the high-anisotropy one: while in the former the agreement is also quantitative, in the latter the mean-field approximation fares worse. In this regard, we may advocate for the presence of strong correlations also in the all-to-all connected model. Even if we find no signs of a second phase transition, we may still argue that the high-anisotropy ferromagnetic regime is physically different from the lower-anisotropy ferromagnet.

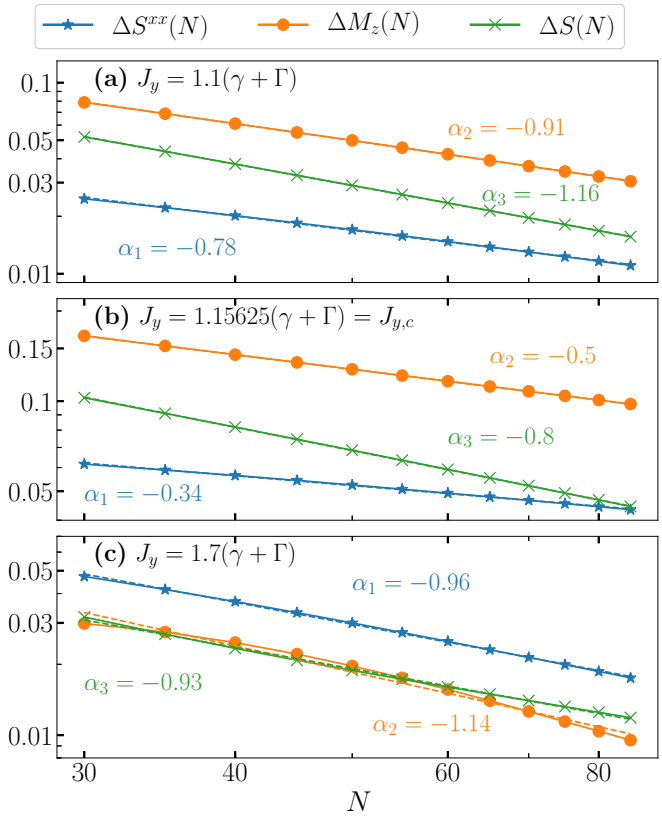

FIG. 11. Study of the system-size scaling, extracted from the quantities plotted in Fig. 10, in the presence of both local and collective dissipation across the paramagnetic-to-ferromagnetic dissipative phase transition. The same conventions as in Fig. 7 are used to refer to the discrepancy between full-quantum simulation and MF prediction for the spin-structure factor, the z magnetization, and the von Neumann entropy. (a) We set $J_y = 1.1\gamma$, (b) $J_y = J_{y,c}$, and (c) $J_y = 1.7\gamma$.

Concerning more technical points, in absence of collective dissipation, we exploit the Liouvillian $\mathbb{PT}$ symmetry [98] to efficiently compute the spectral properties of the Liouvillian superoperator. In the presence of this weak symmetry, the spectrum presents a second symmetry axis beyond the complex-conjugation one. That, in turn, implies the existence of a state symmetric with respect to the steady state, and one associated to the first-excited eigenmatrix of the Liouvillian. The numerical computation of these two states is much easier than finding the real gap and steady state. We thus introduced the antigap of $\mathbb{PT}$-symmetric Liouvillian systems, which is equivalent to the true Liouvillian gap, and thus marks criticality in open quantum systems [15,18].

The possibility to study a large range of spin system sizes allowed us to address the question of how to better characterize the emergence of criticality in finite-size systems. Our results indicate that the physics of systems out of equilibrium is more challenging to infer than one would naively expect, even in the best case scenario of all-to-all connected models, where dimensionality should induce a rapid decrease in correlations and fluctuations. Additionally, we have proven the resilience of the paramagnetic-to-ferromagnetic phase transition in the presence of both local and collective dissipation, finding that the presence of the two mechanisms does not change the nature of the phase transition. In both cases, one observes a second-order phase transition, and the onset of criticality is for the same parameters. These indications are especially relevant to a broad variety of experimental platforms in which the dissipative phase transition can be studied, such as trapped ions, Rydberg atoms, superconducting circuits, and in solid state, especially with hybrid superconducting systems. More generally, these results provide a benchmark for the validity of mean-field approximations in understanding the experimental results obtained with noisy intermediate scale quantum simulators.

As a future outlook, we note that the interplay between local and collective dissipation beyond the all-to-all connected model demands further investigation with the adoption of both analytical and numerical approximate techniques. Exploiting other symmetries, such as translational invariance, it should be possible to further reduce the numerical resources for Liouvillian representation. Moreover, it will be interesting to investigate the system time evolution toward the steady state, as transient processes shall display even starker differences between mean-field or classical results and full quantum dynamics [49,123–128]. Indeed, this study focuses on the steady-state properties of the model, i.e., those which are permutationally invariant. Phenomena breaking this spatial symmetry, however, may arise in the dynamics toward the steady state.

ACKNOWLEDGMENTS

The authors acknowledge useful discussions with A. Biella, G. Piccitto, R. Rota, M. Wauters, and W. Verstraelen. F.M. is supported by the FY2018 JSPS Postdoctoral Fellowship for Research in Japan. F.N. is supported in part by: NTT Research, Army Research Office (ARO) (Grant No. W911NF-18-1-0358), Japan Science and Technology Agency (JST) (via the CREST Grant No. JPMJCR1676), Japan Society for the Promotion of Science (JSPS) (via the KAKENHI Grant No. JP20H00134, JSPS-RFBR Grant No. JPJSBP120194828, and JSPS-FWO Grant No. VS.059.18N), and the Grant No. FQXi-IAF19-06 from the Foundational Questions Institute Fund (FQXi), a donor advised fund of the Silicon Valley Community Foundation. D.H. is supported by UAntwerpen/DOCPRO/34878. Part of the computational resources and services used in this work were provided by the VSC (Flemish Supercomputer Center), funded by the Research Foundation-Flanders (FWO) and the Flemish Government department EWI.

APPENDIX A: LIOUVILLIAN SPECTRUM AND PHASE TRANSITIONS

To obtain the eigenvalues and eigenmatrices introduced in Eq. (5), we can by diagonalizing the matrix representation $\bar{\bar{\mathcal{L}}}$ of the Liouvillian. For the model under consideration,

we have

$$\bar{\bar{\mathcal{L}}} = -i(\hat{H}\otimes\mathbb{1} - \mathbb{1}\otimes\hat{H}^{\mathrm{T}}) + \gamma\sum_{j}^{N}\left(\hat{\sigma}_j^-\otimes\hat{\sigma}_j^- - \frac{\hat{\sigma}_j^+\hat{\sigma}_j^-\otimes\mathbb{1} + \mathbb{1}\otimes\hat{\sigma}_j^+\hat{\sigma}_j^-}{2}\right) + \Gamma\left(\hat{S}^-\otimes\hat{S}^- - \frac{\hat{S}^+\hat{S}^-\otimes\mathbb{1} + \mathbb{1}\otimes\hat{S}^+\hat{S}^-}{2}\right). \quad \text{(A1)}$$

Here, $\hat{A}^T$ represents the transpose of the operator $\hat{A}$. Since this Liouvillian is not Hermitian, in general its eigenvalues λ_i need not to be real. It can be proved that for any Liouvillian, given an eigenvalue λ_i whose eigenmatrix is $\hat{\rho}_i$, there exist a $\hat{\rho}_i^\dagger$ whose eigenvalue is λ_i^* [18]. Therefore, the eigenvalues are symmetrically distributed with respect to the real axis, as shown in Fig. 2. Moreover, they are characterized by $\mathrm{Re}[\lambda_i] \leqslant 0$. We order the eigenvalues λ_i in such a way that $|\mathrm{Re}[\lambda_0]| < |\mathrm{Re}[\lambda_1]| < \cdots < |\mathrm{Re}[\lambda_n]| < \cdots$, i.e., the eigenvalues are ordered by their real part. In this regard, the steady state, that is the density matrix $\hat{\rho}_{\mathrm{ss}}$ such that $\mathcal{L}\hat{\rho}_{\mathrm{ss}} = 0$, is the eigenmatrix of the Liouvillian associated to the zero eigenvalue. The real part of the eigenvalues describes the relaxation toward the steady state of a generic matrix, while the complex part describes the oscillatory processes which may take place.

Symmetry breaking and phase transition

The Lindblad master equation (2) is invariant under a π rotation of all the spins around the z axis ($\hat{\sigma}_i^x \to -\hat{\sigma}_i^x$, $\hat{\sigma}_i^y \to -\hat{\sigma}_i^y$ $\forall\, i$). Thus, the system admits a $\mathcal{Z}_2$ symmetry, that is, there is a superoperator $\mathcal{Z}_2$ such that

$$\mathcal{Z}_2\hat{\rho}(t) = \prod_{j=1}^{N}\exp\left(-i\pi\hat{\sigma}_j^z\right)\hat{\rho}(t)\prod_{j'=1}^{N}\exp\left(+i\pi\hat{\sigma}_{j'}^z\right), \quad \text{(A2)}$$

and one can verify that $[\mathcal{L}, \mathcal{Z}_2] = 0$. While in a Hamiltonian system the presence of a symmetry implies a conserved quantity, this is not always the case for Liouvillian symmetries [129–132]. A symmetry of an out-of-equilibrium system, however, implies that the steady state cannot have an arbitrary structure. In our case, $\hat{\rho}_{\mathrm{ss}}$ must be an eigenmatrix of $\mathcal{Z}_2$, such that $\mathcal{Z}_2\hat{\rho}_{\mathrm{ss}} \propto \hat{\rho}_{\mathrm{ss}}$. In turn, this means that, for any finite-size system $\langle\hat{\sigma}_i^x\rangle = \langle\hat{\sigma}_i^y\rangle = 0$ for all sites i.

The symmetry breaking takes place when, in the thermodynamic limit, $\lambda_1 = 0$ allows to have two steady states with nonzero and opposite magnetization. We thus expect to observe a second-order phase transition associated to this symmetry breaking of $\mathcal{Z}_2$ [18]. For a finite-size system $\lambda_1 \neq 0$, such symmetry breaking cannot be directly witnessed. However, the precursors of the phase transition can be inferred both via spectral analysis and via an extensive study of the scaling of observables.

APPENDIX B: FINITE-SIZE SCALING AND EFFECTS

Throughout this work, a finite-size scaling is used to study the behavior of the system in the thermodynamic limit. That is, we exploit the presence of clear functional dependence of observables on the size N of the system to argue about the critical properties in the thermodynamic limit $N \to \infty$. This extrapolation to infinite system size allows us to use the terminology of phase transitions. It is worth noting that the presence of clear functional dependencies on system size do not exclude artifacts due to the finite system size. These artifacts are often called finite-size effects and they disappear as the system becomes larger. A few examples of finite-size effects present in this work are as follows:

(i) the Liouvillian gap never being exactly zero;

(ii) the change of the position of the minimum of the Liouvillian gap $\min(\lambda(N))$, with N;

(iii) the angular-averaged susceptibility never being infinite;

(iv) the change of the position of the divergence in the angular-averaged susceptibility with N.

The influence of these finite-size effects on the system size can vary for different physical quantities, i.e., they become negligible at different system sizes. As an example, we can look at the Liouvillian gap, shown in Fig. 3. Our analysis allows us to find a clear power-law scaling of $\min(\lambda(N)) \propto N^{-0.3}$, i.e., the slowest timescale diverges by increasing the system size, signaling a phase transition. However, the determination of the position of this minimum is not possible for the observed system sizes.

We can thus determine the value of the Liouvillian gap in the thermodynamic limit but we cannot precisely infer from its study the critical coupling parameter $J_{y,c}$. This shows that finite-size effects for different quantities can persevere for bigger system sizes. A similar conclusion can be found for the angular-averaged susceptibility in Fig. 8, where the divergence of the maximum indicates the presence of a second-order phase transition but we cannot determine the critical coupling parameter $J_{y,c}$ solely from that analysis. To remedy the shortcomings raised by these finite-size effects, one has to study various physical quantities that can circumvent the specific finite-size effects. An example in this work is the use of the bimodality coefficient to pinpoint the location of the transition, Sec. V B.

APPENDIX C: COLLECTIVE DISSIPATION ONLY: SYMMETRY AND RELATION WITH SUPERRADIANT LIGHT-MATTER MODELS

In the main text, we mainly consider the presence of either local and collective dissipation, or only of the local one. Here, let us briefly consider the properties of the system in the presence of collective dissipation only, $\Gamma \neq 0$ and $\gamma = 0$ in Eq. (2) [46,47,49].

In this case, the total spin length

$$\hat{S}^2 = (\hat{S}^x)^2 + (\hat{S}^y)^2 + (\hat{S}^z)^2 \quad \text{(C1)}$$

is a conserved quantity

$$[\hat{S}^2, \hat{H}] = [\hat{S}^2, \hat{S}^-] = 0, \quad \text{(C2)}$$

and therefore the presence of conserved quantities implies the existence of several steady states for the Lindbladian dynamics [129–131]. In more physical terms, this indicates that there exist different multiplets, which are eigenstates of $\hat{S}^2$, that are not connected by the dissipative dynamics. These multiplets are known as Dicke ladders [133].

This terminology is inherited from the study of the Dicke model. The similarities between the all-to-all connected *XYZ*

and Dicke models are both due to mathematical similarities, which become even more apparent when exploiting the permutational symmetry, and because this is another benchmark model thoroughly used to investigate both quantum phase transitions and dissipative phase transitions, this time in the field of cavity QED and quantum optics [49], instead of spin models.

Describing the collective interaction between an ensemble of two-level systems with a unique photonic field, the Dicke model is known to display superradiant photon emission in the presence of collective dissipation [134–136]. Superradiance is also known to occur in crystals of molecular nanomagnets [137]. Here, with superradiant emission we refer to the fact that the light emission intensity scales as N^2 and occurs on a timescale that shrinks with the size of the system, a macroscopic manifestation of cooperative behavior. Note that this phenomenon does not require any strong coupling between light and matter to occur (differently from the superradiant phase transitions), so that one can map the light-matter model to an effective spin model that fulfils Eq. (C2), with $\hat{H} = \omega_z \hat{S}^z$, where ω_z is the resonance frequency. Superradiance has also recently been experimentally observed in novel optical materials, such as erbium-doped yttrium orthosilicate [138] and lead halide perovskite [139].

Note that, in the presence of collective coupling only, a Holstein-Primakoff transformation can be performed to map the system to a bosonic model [140], whose first-order approximation is valid in the low-excitation regime and is good in the thermodynamic limit. The main assumption of coupling only to a collective field is based on the assumption of identical two-level systems (spins) and their identical coupling to the photonic field. When these assumptions are relaxed, intermediate superradiant regimes can still be obtained [15,19,141–144], resulting from the population of different Dicke ladders [145,146], experimentally verified in solid-state systems [103,108,110]. In that case, a bosonic approximation in terms of polaritonic populations can be performed, but only in the low-excitation regime [146,147]. In the presence of local incoherent pumping and collective dissipation, the superradiant phase [148] and steady-state superradiant emission [149] have been proposed and observed in cavity-QED setups with atomic clouds [150,151]. Similarly, trapped ions and atomic lattices provide the opportunity to engineer long-range interactions and dissipation [152,153], relevant also for the implementation of the anisotropic Heisenberg models [154].

APPENDIX D: EXPLOITING THE PERMUTATIONAL SYMMETRY IN THE PRESENCE OF HOMOGENEOUS LOCAL DISSIPATION

From a computational point of view, the numerical solution of the master equation (2) is a formidable task when considering extended lattices. The density matrix for N spins lives in a 2^N-dimensional Hilbert space. If one were interested only in the Hamiltonian unitary dynamics, the Hilbert space dimension reduces to $(N+1)$, at most, using the basis of collective spin states. These are the Dicke states $|j,m\rangle$, where j is the cooperation number of the collective spin length and m its projection along one of the axes ($0 \leqslant j \leqslant \frac{N}{2}$ and $|m| \leqslant j$, both are integer or semi-integer numbers).

However, in general, considering local dissipation to separate environments in the Lindblad master equation (2) requires storing a matrix of size $4^N \times 4^N$. If one assumes that each spin dissipates at the same rate γ, the system possesses permutational symmetry also in Liouvillian space [92]. The presence of local dissipation connects spin multiplets with different cooperation number j. The description of the dynamics can still be performed using only $O(N^3)$ computational resources, as detailed in Ref. [92].

For numerical purposes, one of the key features of the density matrix of the collective system is its block-diagonal structure, arising from the fact that permutational invariance forbids coherences between matrix elements $\rho_{j,m;j'm'} = \langle j', m'|\hat{\rho}|j,m\rangle$ for $j \neq j'$. This allows to consider the matrix $\hat{\rho}_{j,m,m'} = \bigoplus_{j=j_{\min}}^{N/2} \hat{\rho}_j$, where each block $\hat{\rho}_j$ has dimension $(2j+1)\times(2j+1)$ through which m and m' run, and $j_{\min}$ is either 0 or $\frac{1}{2}$ for even or odd number of spins, respectively. There are thus $O(N^2)$ matrix elements in each block for $O(N)$ blocks, making the number of elements required to characterize $\hat{\rho}$ only $O(N^3)$. This matrix representation exploits the fact that, for each block $\hat{\rho}_j$, there are actually $d_j^{(N)}$ identical blocks with the same matrix elements [92,155]

$$d_j^{(N)} = (2j+1)\frac{N!}{\left(\frac{N}{2}+j+1\right)!\left(\frac{N}{2}-j\right)!}. \tag{D1}$$

When one calculates collective properties based on operator expectation values $\langle A\rangle = \mathrm{Tr}[A\hat{\rho}]$, the average over identical blocks is implicit due to the linearity of the trace: one can neglect the degeneracy, Eq. (D1), and directly compute the expectation values.

However, in order to calculate quantities obtained from the trace of *nonlinear* functions of the density matrix $f[\hat{\rho}]$, such as the von Neumann entropy $S[\hat{\rho}] = \mathrm{Tr}[\hat{\rho}\ln(\hat{\rho})]$ or the purity $\mu[\hat{\rho}] = \mathrm{Tr}[\hat{\rho}^2]$, it is necessary to account for the degeneracy of each block of such block-diagonal density matrix, weighting the contribution of each degenerate block with the factor $d_j^{(N)}$ of Eq. (D1):

$$f[\hat{\rho}_{j,m,m'}] = \sum_{j=j_{\min}}^{N/2} d_j^{(N)} \mathrm{Tr}\left[f\left[\hat{\rho}_j/d_j^{(N)}\right]\right]. \tag{D2}$$

APPENDIX E: CALCULATION OF PHYSICAL QUANTITIES

In this Appendix we introduce the general definitions of the spin-structure factor, z magnetization, and von Neumann entropy, also providing their mean-field expressions. We also give more details about the bimodality coefficient and the angular-averaged susceptibility.

1. Spin-structure factor and z magnetization

To identify the possible agreement of the mean-field theory with the exact numerical solutions, we study the order parameter of the system. Due to the $\mathcal{Z}_2$ symmetry present in the system, we cannot rely on the magnetization in the x and y directions. As a result, we study the steady-state spin-structure

factor, which is calculated as follows:

$$S^{\alpha\beta}(\mathbf{k}) = \frac{1}{N(N-1)} \sum_{j \neq l} e^{i\mathbf{k}\cdot(\mathbf{j}-\mathbf{l})} \langle \hat{\sigma}_j^{\alpha} \hat{\sigma}_l^{\beta} \rangle, \tag{E1}$$

where α, $\beta = x$ or y and where $\langle \hat{\sigma}_j^{\alpha} \hat{\sigma}_l^{\beta} \rangle = \mathrm{Tr}[\hat{\sigma}_j^{\alpha} \hat{\sigma}_l^{\beta} \hat{\rho}_{\mathrm{ss}}]$. It contains information on the orientation of the spins with respect to each other. Ferromagnetic order is present in the xy plane if the steady-state spin-structure factor in the x direction or (and) the y direction is different from zero.

We note that in Eq. (E1) the spin-structure factor is defined without the contribution of the self-energies, i.e., the sum over the sites considers only different spins. We can thus calculate these quantities even for permutational-symmetric systems, subtracting the single-site contributions to the total second moments.

If we consider $S^{xx}(\mathbf{k} = 0)$ or $S^{yy}(\mathbf{k} = 0)$ (here and in the main text we drop the $\mathbf{k} = 0$), they predict a ferromagnetic phase when they are nonzero and a paramagnetic phase when they are both equal to zero. Aside from being able to identify the phase, we are also interested in the quantitative agreement of the mean-field theory with the exact solutions. To this end, we also study the z magnetization in the steady state $M_z = \mathrm{Tr}[\hat{\rho}_{\mathrm{ss}} \hat{S}^z]/N$, which can be readily calculated without the limitations of the $\mathcal{Z}_2$ symmetry.

Mean-field spin-structure factor and z magnetization

The system of mean-field equations in Eq. (E2) is analytically solvable for the steady state. By equating the time derivative equal to zero we find the following solutions for the magnetization in each direction:

$$M_{x\,\mathrm{MF}} = \pm \sqrt{2M_{z\,\mathrm{MF}}(M_{z\,\mathrm{MF}} + 1)\frac{J_y - J_z}{J_x - J_y}}, \tag{E2a}$$

$$M_{y\,\mathrm{MF}} = \mp \sqrt{2M_{z\,\mathrm{MF}}(M_{z\,\mathrm{MF}} + 1)\frac{J_z - J_x}{J_x - J_y}}, \tag{E2b}$$

$$M_{z\,\mathrm{MF}} = -\frac{\gamma}{4} \frac{1}{\sqrt{(J_y - J_z)(J_z - J_x)}}. \tag{E2c}$$

One can also easily prove that the steady-state spin-structure factor in the x direction can be written as

$$S^{xx}_{\mathrm{MF}} = (M_{x\,\mathrm{MF}})^2 = 2M_{z\,\mathrm{MF}}(M_{z\,\mathrm{MF}} + 1)\frac{J_y - J_z}{J_x - J_y} \tag{E3}$$

by using the Gutzwiller mean-field properties. The calculation in the y direction is analog.

2. Von Neumann entropy

The study of the von Neumann entropy of the steady state is an interesting extension of our previous analysis since in standard thermodynamics a second-order phase transition is associated to a change in the entropy of the system. The von Neumann entropy reads as

$$S = -\sum_i p_i \ln(p_i), \tag{E4}$$

with p_i the eigenvalues of the density matrix. It can thus provide information on the mixed nature of the steady-state density matrix $\hat{\rho}_{\mathrm{ss}}$. Usually in many-body studies one is able to calculate this observable only for small systems. However, similarly to the other variables in this work, we are able to calculate it up to the order of $N = 95$ spins. The von Neumann entropy is an extensive quantity and in the main text we study the von Neumann entropy per spin: $S(N)/N$.

Mean-field von Neumann entropy

The mean-field entropy can be calculated by noting that the density matrix can be written in its Bloch sphere representation $\hat{\rho} = \frac{1}{2}(\mathbb{1} + \vec{\epsilon} \cdot \vec{\hat{\sigma}})$. With $\vec{\epsilon}$ the Bloch vector, which contains the magnetization in the x, y, and z directions, and $\hat{\sigma}$ the Pauli matrices. The eigenvalues are given by $p = (1 \pm |\vec{\epsilon}|)/2$. These eigenvalues can be readily calculated from the steady-state mean-field equations (E2) and give access to the MF approximation of the von Neumann entropy through (E4):

$$\frac{S_{\mathrm{MF}}}{N} = -\frac{(1+J)}{2} \ln\left(\frac{(1+J)}{2}\right) - \frac{(1-J)}{2} \ln\left(\frac{(1-J)}{2}\right), \tag{E5}$$

where $J^2 = \langle \hat{S}^2 \rangle = \mathrm{Tr}[\hat{S}^2 \hat{\rho}(t)]$ is the expectation value of the total spin length [cf. Eq. (C1)] in the mean-field approximation.

The von Neumann entropy solely depends on J in Eq. (E5), illustrating the fact that states with maximum cooperation number, lying on the surface of the Bloch sphere, have minimum entropy. Instead, the entropy increases with decreasing spin length until the value $S_{\mathrm{MF}}/N = \ln(2)$, which is indeed the maximum entropy of a qubit. In particular, we can express Eq. (E5) explicitly in terms of the steady-state values $\langle \hat{\sigma}^x \rangle_{\mathrm{ss}}$, $\langle \hat{\sigma}^y \rangle_{\mathrm{ss}}$, and $\langle \hat{\sigma}^z \rangle_{\mathrm{ss}}$. These results would be true independently of the model under consideration and even for the system dynamics, given the nature of the Gutzwiller mean-field ansatz for two-level systems $\langle \hat{\sigma}_i^z \hat{\sigma}_j^z \rangle_{\mathrm{ss}} \approx \langle \hat{\sigma}^z \rangle_{\mathrm{ss}}^2$.

3. Bimodality coefficient

Using the permutational invariance present in this system, one is able to calculate results for a higher number of spins than usually feasible with other techniques. However, as noted before, finite-size effects are still present, hampering our ability to make a good estimate of the point of transition from the paramagnetic to the ferromagnetic phase using the order parameter. An indicator which is extremely suited for making a good estimate of this transition point is the bimodality coefficient, defined as

$$B_c = \frac{m_2^2}{m_4}, \tag{E6}$$

with m_n being the nth moment of an observable. The bimodality coefficient gives information on the bimodal nature of the operator used to calculate the moments. This bimodal nature indicates the presence of a ferromagnetic phase or a paramagnetic phase. A bimodal distribution for $\sum_i \sigma_i^x$, being the magnetization in the x direction, indicates a ferromagnetic phase and typically has values close to $B_c = 1$. A paramagnetic phase, i.e., a unimodal distribution, is indicated by smaller values for B_c. A Gaussian distribution with zero

mean has a value $B_c = \frac{1}{3}$ [55,156]. Note that the bimodality coefficient is closely related to the Binder cumulant [157,158].

Aside from information on the nature of the phases at a specific parameter, the bimodality coefficient can also be used to indicate the transition point between the different phases. The curves for the bimodality coefficient for different system sizes intersect, providing an estimate of the critical point. In finite-size systems, these intersection points coincide due to power-law dependence of correlations on the system size around the critical point. In our case, since different number of spins correspond to different dimensions, this intersection point changes. However, for sufficiently large systems, this transition point should converge, indicating the phase transition.

We are interested in the presence of a ferromagnetic or paramagnetic phase in the xy plane, and as such we study the emergence of ferromagnetic order in either the x or y direction. The second and fourth moments of $\hat{\sigma}_i^x$ and $\hat{\sigma}_i^y$ are readily calculated in the new basis, as they are expectation values of global operators.

4. Angular-averaged susceptibility

If a small magnetic field of intensity h is applied in the xy plane as a probe,

$$\hat{H}_B(h,\theta) = h\sum_i \left[\cos(\theta)\hat{\sigma}_i^x + \sin(\theta)\hat{\sigma}_i^y\right], \tag{E7}$$

it explicitly breaks the $\mathcal{Z}_2$ symmetry of the system. By obtaining the perturbed steady state $\hat{\rho}(h,\theta)$ for $\hat{H}_{\rm ext}(h,\theta) = \hat{H} + \hat{H}_B(h,\theta)$, the resulting magnetization reads as

$$M_\alpha = \frac{1}{N}\sum_{j=1}^{N} \mathrm{Tr}\left[\hat{\rho}(h,\theta)\hat{\sigma}_j^\alpha\right], \quad \alpha = x,\ y. \tag{E8}$$

Calling $h_x = h\cos(\theta)$ and $h_y = h\sin(\theta)$, the magnetic response in the linear regime is

$$\vec{M}(h,\theta) = \begin{pmatrix} \chi_{xx} & \chi_{xy} \\ \chi_{yx} & \chi_{yy} \end{pmatrix} \begin{pmatrix} h\cos(\theta) \\ h\sin(\theta) \end{pmatrix}, \tag{E9}$$

where the susceptibility tensor is defined as

$$\chi_{\alpha\beta} = \left.\frac{\partial M_\alpha}{\partial h_\beta}\right|_{h\to 0}. \tag{E10}$$

A scalar value can be obtained from this susceptibility tensor through angular averaging of the determinant, i.e.,

$$\chi_{\rm av} = \frac{1}{2\pi}\int_0^{2\pi} \left.\frac{\partial|\vec{M}(h,\theta)|}{\partial h}\right|_{h\to 0} d\theta. \tag{E11}$$

The mean-field angular-averaged susceptibility can be calculated through numerically solving the mean-field equations with an applied field as stipulated above and also applying Eq. (E11).

[1] S. Haroche and J. M. Raimond, *Exploring the Quantum: Atoms, Cavities, and Photons* (Oxford University Press, Oxford, 2006).

[2] H. Breuer and F. Petruccione, *The Theory of Open Quantum Systems* (Oxford University Press, Oxford, 2007).

[3] H. J. Carmichael, *Statistical Methods in Quantum Optics 1: Master Equations and Fokker-Planck Equations* (Springer, Berlin, 1999).

[4] R. J. Schoelkopf and S. M. Girvin, Wiring up quantum systems, Nature (London) **451**, 664 (2008).

[5] J. Q. You and F. Nori, Atomic physics and quantum optics using superconducting circuits, Nature (London) **474**, 589 (2011).

[6] B. Deveaud, *The Physics of Semiconductor Microcavities: From Fundamentals to Nanoscale Devices* (Wiley, New York, 2007).

[7] A. Kavokin, J. J. Baumberg, G. Malpuech, and F. P. Laussy, *Microcavities* (Oxford University Press, Oxford, 2007).

[8] D. Ballarini and S. De Liberato, Polaritonics: From microcavities to sub-wavelength confinement, Nanophotonics **8**, 641 (2019).

[9] M. Aspelmeyer, T. J. Kippenberg, and F. Marquardt, Cavity optomechanics, Rev. Mod. Phys. **86**, 1391 (2014).

[10] J. J. Hopfield, Theory of the contribution of excitons to the complex dielectric constant of crystals, Phys. Rev. **112**, 1555 (1958).

[11] C. Ciuti, P. Schwendimann, and A. Quattropani, Theory of polariton parametric interactions in semiconductor microcavities, Semicond. Sci. Technol. **18**, S279 (2003).

[12] I. Carusotto and C. Ciuti, Quantum fluids of light, Rev. Mod. Phys. **85**, 299 (2013).

[13] L. D. Landau and E. M. Lifshitz, *Statistical Physics*, Course of Theoretical Physics (Elsevier, Amsterdam, 2013), Vol. 5.

[14] S. Sachdev, *Quantum Phase Transitions* (Cambridge University Press, Cambridge, 2001).

[15] E. M. Kessler, G. Giedke, A. Imamoglu, S. F. Yelin, M. D. Lukin, and J. I. Cirac, Dissipative phase transition in a central spin system, Phys. Rev. A **86**, 012116 (2012).

[16] E. G. Dalla Torre, E. Demler, T. Giamarchi, and E. Altman, Dynamics and universality in noise-driven dissipative systems, Phys. Rev. B **85**, 184302 (2012).

[17] J. Marino and S. Diehl, Driven Markovian Quantum Criticality, Phys. Rev. Lett. **116**, 070407 (2016).

[18] F. Minganti, A. Biella, N. Bartolo, and C. Ciuti, Spectral theory of Liouvillians for dissipative phase transitions, Phys. Rev. A **98**, 042118 (2018).

[19] P. Kirton and J. Keeling, Suppressing and Restoring the Dicke Superradiance Transition by Dephasing and Decay, Phys. Rev. Lett. **118**, 123602 (2017).

[20] P. Kirton, M. M. Roses, J. Keeling, and E. G. Dalla Torre, Introduction to the Dicke model: From equilibrium to nonequilibrium, and vice versa, Adv. Quantum Technol. **2**, 1800043 (2019).

[21] S. Diehl, A. Micheli, A. Kantian, B. Kraus, H. P. Büchler, and P. Zoller, Quantum states and phases in driven open quantum systems with cold atoms, Nat. Phys. **4**, 878 (2008).

[22] F. Verstraete, M. M. Wolf, and J. I. Cirac, Quantum computation and quantum-state engineering driven by dissipation, Nat. Phys. **5**, 633 (2009).

[23] N. Lambert, Y.-n. Chen, R. Johansson, and F. Nori, Quantum chaos and critical behavior on a chip, Phys. Rev. B **80**, 165308 (2009).

[24] S. Diehl, A. Tomadin, A. Micheli, R. Fazio, and P. Zoller, Dynamical Phase Transitions and Instabilities in Open Atomic Many-Body Systems, Phys. Rev. Lett. **105**, 015702 (2010).

[25] T. E. Lee, S. Gopalakrishnan, and M. D. Lukin, Unconventional Magnetism Via Optical Pumping of Interacting Spin Systems, Phys. Rev. Lett. **110**, 257204 (2013).

[26] J. Iles-Smith, N. Lambert, and A. Nazir, Environmental dynamics, correlations, and the emergence of noncanonical equilibrium states in open quantum systems, Phys. Rev. A **90**, 032114 (2014).

[27] J. Jin, A. Biella, O. Viyuela, L. Mazza, J. Keeling, R. Fazio, and D. Rossini, Cluster Mean-Field Approach to the Steady-State Phase Diagram of Dissipative Spin Systems, Phys. Rev. X **6**, 031011 (2016).

[28] H. J. Carmichael, Breakdown of Photon Blockade: A Dissipative Quantum Phase Transition in Zero Dimensions, Phys. Rev. X **5**, 031028 (2015).

[29] H. Weimer, Variational Principle for Steady States of Dissipative Quantum Many-Body Systems, Phys. Rev. Lett. **114**, 040402 (2015).

[30] M. Benito, C. Sánchez Muñoz, and C. Navarrete-Benlloch, Degenerate parametric oscillation in quantum membrane optomechanics, Phys. Rev. A **93**, 023846 (2016).

[31] J. J. Mendoza-Arenas, S. R. Clark, S. Felicetti, G. Romero, E. Solano, D. G. Angelakis, and D. Jaksch, Beyond mean-field bistability in driven-dissipative lattices: Bunching-antibunching transition and quantum simulation, Phys. Rev. A **93**, 023821 (2016).

[32] W. Casteels, F. Storme, A. Le Boité, and C. Ciuti, Power laws in the dynamic hysteresis of quantum nonlinear photonic resonators, Phys. Rev. A **93**, 033824 (2016).

[33] N. Bartolo, F. Minganti, W. Casteels, and C. Ciuti, Exact steady state of a Kerr resonator with one- and two-photon driving and dissipation: Controllable Wigner-function multimodality and dissipative phase transitions, Phys. Rev. A **94**, 033841 (2016).

[34] W. Casteels and C. Ciuti, Quantum entanglement in the spatial-symmetry-breaking phase transition of a driven-dissipative Bose-Hubbard dimer, Phys. Rev. A **95**, 013812 (2017).

[35] W. Casteels, R. Fazio, and C. Ciuti, Critical dynamical properties of a first-order dissipative phase transition, Phys. Rev. A **95**, 012128 (2017).

[36] M. Foss-Feig, P. Niroula, J. T. Young, M. Hafezi, A. V. Gorshkov, R. M. Wilson, and M. F. Maghrebi, Emergent equilibrium in many-body optical bistability, Phys. Rev. A **95**, 043826 (2017).

[37] M. Biondi, G. Blatter, H. E. Türeci, and S. Schmidt, Nonequilibrium gas-liquid transition in the driven-dissipative photonic lattice, Phys. Rev. A **96**, 043809 (2017).

[38] A. Biella, F. Storme, J. Lebreuilly, D. Rossini, R. Fazio, I. Carusotto, and C. Ciuti, Phase diagram of incoherently driven strongly correlated photonic lattices, Phys. Rev. A **96**, 023839 (2017).

[39] V. Savona, Spontaneous symmetry breaking in a quadratically driven nonlinear photonic lattice, Phys. Rev. A **96**, 033826 (2017).

[40] C. Sánchez Muñoz, A. Lara, J. Puebla, and F. Nori, Hybrid Systems for the Generation of Nonclassical Mechanical States via Quadratic Interactions, Phys. Rev. Lett. **121**, 123604 (2018).

[41] F. Vicentini, F. Minganti, R. Rota, G. Orso, and C. Ciuti, Critical slowing down in driven-dissipative Bose-Hubbard lattices, Phys. Rev. A **97**, 013853 (2018).

[42] W. Verstraelen and M. Wouters, Gaussian quantum trajectories for the variational simulation of open quantum-optical systems, Appl. Sci. **8**, 1427 (2018).

[43] L. M. Sieberer, S. D. Huber, E. Altman, and S. Diehl, Dynamical Critical Phenomena in Driven-Dissipative Systems, Phys. Rev. Lett. **110**, 195301 (2013).

[44] L. M. Sieberer, S. D. Huber, E. Altman, and S. Diehl, Nonequilibrium functional renormalization for driven-dissipative Bose-Einstein condensation, Phys. Rev. B **89**, 134310 (2014).

[45] E. Altman, L. M. Sieberer, L. Chen, S. Diehl, and J. Toner, Two-Dimensional Superfluidity of Exciton Polaritons Requires Strong Anisotropy, Phys. Rev. X **5**, 011017 (2015).

[46] S. Morrison and A. S. Parkins, Collective spin systems in dispersive optical cavity QED: Quantum phase transitions and entanglement, Phys. Rev. A **77**, 043810 (2008).

[47] S. Morrison and A. S. Parkins, Dynamical Quantum Phase Transitions in the Dissipative Lipkin-Meshkov-Glick Model with Proposed Realization in Optical Cavity Qed, Phys. Rev. Lett. **100**, 040403 (2008).

[48] T. E. Lee, H. Häffner, and M. C. Cross, Antiferromagnetic phase transition in a nonequilibrium lattice of Rydberg atoms, Phys. Rev. A **84**, 031402(R) (2011).

[49] T. E. Lee, C.-K. Chan, and S. F. Yelin, Dissipative phase transitions: Independent versus collective decay and spin squeezing, Phys. Rev. A **90**, 052109 (2014).

[50] C. K. Chan, T. E. Lee, and S. Gopalakrishnan, Limit-cycle phase in driven-dissipative spin systems, Phys. Rev. A **91**, 051601(R) (2015).

[51] M. F. Maghrebi and A. V. Gorshkov, Nonequilibrium many-body steady states via Keldysh formalism, Phys. Rev. B **93**, 014307 (2016).

[52] R. Rota, F. Storme, N. Bartolo, R. Fazio, and C. Ciuti, Critical behavior of dissipative two-dimensional spin lattices, Phys. Rev. B **95**, 134431 (2017).

[53] V. R. Overbeck, M. F. Maghrebi, A. V. Gorshkov, and H. Weimer, Multicritical behavior in dissipative Ising models, Phys. Rev. A **95**, 042133 (2017).

[54] D. Roscher, S. Diehl, and M. Buchhold, Phenomenology of first-order dark-state phase transitions, Phys. Rev. A **98**, 062117 (2018).

[55] R. Rota, F. Minganti, A. Biella, and C. Ciuti, Dynamical properties of dissipative XYZ Heisenberg lattices, New J. Phys. **20**, 045003 (2018).

[56] H. Landa, M. Schiró, and G. Misguich, Multistability of Driven-Dissipative Quantum Spins, Phys. Rev. Lett. **124**, 043601 (2020).

[57] J. M. Fink, A. Dombi, A. Vukics, A. Wallraff, and P. Domokos, Observation of the Photon-Blockade Breakdown Phase Transition, Phys. Rev. X **7**, 011012 (2017).

[58] A. A. Houck, H. E. Tureci, and J. Koch, On-chip quantum simulation with superconducting circuits, Nat. Phys. **8**, 292 (2012).

[59] M. Fitzpatrick, N. M. Sundaresan, A. C. Y. Li, J. Koch, and A. A. Houck, Observation of a Dissipative Phase Transition in a One-Dimensional Circuit QED Lattice, Phys. Rev. X **7**, 011016 (2017).

[60] M. Müller, S. Diehl, G. Pupillo, and P. Zoller, Engineered open systems and quantum simulations with atoms and ions, Adv. At., Mol., Opt. Phys. **61**, 1 (2012).

[61] H. Bernien, S. Schwartz, A. Keesling, H. Levine, A. Omran, H. Pichler, S. Choi, A. S. Zibrov, M. Endres, M. Greiner, V. Vuletić, and M. D. Lukin, Probing many-body dynamics on a 51-atom quantum simulator, Nature (London) **551**, 579 (2017).

[62] E. Gil-Santos, M. Labousse, C. Baker, A. Goetschy, W. Hease, C. Gomez, A. Lemaître, G. Leo, C. Ciuti, and I. Favero, Light-Mediated Cascaded Locking of Multiple Nano-Optomechanical Oscillators, Phys. Rev. Lett. **118**, 063605 (2017).

[63] J. Kasprzak, M. Richard, S. Kundermann, A. Baas, P. Jeambrun, J. M. J. Keeling, F. M. Marchetti, M. H. Szymanska, R. Andre, J. L. Staehli, V. Savona, P. B. Littlewood, B. Deveaud, and L. S. Dang, Bose-Einstein condensation of exciton polaritons, Nature (London) **443**, 409 (2006).

[64] S. R. K. Rodriguez, W. Casteels, F. Storme, N. Carlon Zambon, I. Sagnes, L. Le Gratiet, E. Galopin, A. Lemaître, A. Amo, C. Ciuti, and J. Bloch, Probing a Dissipative Phase Transition via Dynamical Optical Hysteresis, Phys. Rev. Lett. **118**, 247402 (2017).

[65] T. Fink, A. Schade, S. Höfling, C. Schneider, and A. Imamoglu, Signatures of a dissipative phase transition in photon correlation measurements, Nat. Phys. **14**, 365 (2018).

[66] A. D. Greentree, C. Tahan, J. H. Cole, and L. C. L. Hollenberg, Quantum phase transitions of light, Nat. Phys. **2**, 856 (2006).

[67] M. J. Hartmann, F. G. S. L. Brandão, and M. B. Plenio, Strongly interacting polaritons in coupled arrays of cavities, Nat. Phys. **2**, 849 (2006).

[68] D. G. Angelakis, M. F. Santos, and S. Bose, Photon-blockade-induced Mott transitions and *xy* spin models in coupled cavity arrays, Phys. Rev. A **76**, 031805(R) (2007).

[69] M. J. Hartmann, F. G. S. L. Brandão, and M. B. Plenio, Quantum many-body phenomena in coupled cavity arrays, Laser Photonics Rev. **2**, 527 (2008).

[70] J. Lebreuilly, A. Biella, F. Storme, D. Rossini, R. Fazio, C. Ciuti, and I. Carusotto, Stabilizing strongly correlated photon fluids with non-Markovian reservoirs, Phys. Rev. A **96**, 033828 (2017).

[71] M. Greiner, O. Mandel, T. Esslinger, T. W. Hänsch, and I. Bloch, Quantum phase transition from a superfluid to a Mott insulator in a gas of ultracold atoms, Nature (London) **415**, 39 (2002).

[72] I. Bloch, J. Dalibard, and W. Zwerger, Many-body physics with ultracold gases, Rev. Mod. Phys. **80**, 885 (2008).

[73] H. J. Carmichael, Photon Antibunching and Squeezing for a Single Atom in a Resonant Cavity, Phys. Rev. Lett. **55**, 2790 (1985).

[74] A. Imamoglu, H. Schmidt, G. Woods, and M. Deutsch, Strongly Interacting Photons in a Nonlinear Cavity, Phys. Rev. Lett. **79**, 1467 (1997).

[75] A. Miranowicz, M. Paprzycka, Y.-x. Liu, J. Bajer, and F. Nori, Two-photon and three-photon blockades in driven nonlinear systems, Phys. Rev. A **87**, 023809 (2013).

[76] A. Kowalewska-Kudłaszyk, S. I. Abo, G. Chimczak, J. Peřina, F. Nori, and A. Miranowicz, Two-photon blockade and photon-induced tunneling generated by squeezing, Phys. Rev. A **100**, 053857 (2019).

[77] K. M. Birnbaum, A. Boca, R. Miller, A. D. Boozer, T. E. Northup, and H. J. Kimble, Photon blockade in an optical cavity with one trapped atom, Nature (London) **436**, 87 (2005).

[78] C. Lang, D. Bozyigit, C. Eichler, L. Steffen, J. M. Fink, A. A. Abdumalikov, M. Baur, S. Filipp, M. P. da Silva, A. Blais, and A. Wallraff, Observation of Resonant Photon Blockade at Microwave Frequencies using Correlation Function Measurements, Phys. Rev. Lett. **106**, 243601 (2011).

[79] M. J. Hartmann, F. G. S. L. Brandão, and M. B. Plenio, Effective Spin Systems in Coupled Microcavities, Phys. Rev. Lett. **99**, 160501 (2007).

[80] A. Kay and D. G. Angelakis, Reproducing spin lattice models in strongly coupled atom-cavity systems, Europhys. Lett. **84**, 20001 (2008).

[81] S. Puri, C. K. Andersen, A. L. Grimsmo, and A. Blais, Quantum annealing with all-to-all connected nonlinear oscillators, Nat. Commun. **8**, 15785 (2017).

[82] J. Qian, G. Dong, L. Zhou, and W. Zhang, Phase diagram of Rydberg atoms in a nonequilibrium optical lattice, Phys. Rev. A **85**, 065401 (2012).

[83] M. Viteau, P. Huillery, M. G. Bason, N. Malossi, D. Ciampini, O. Morsch, E. Arimondo, D. Comparat, and P. Pillet, Cooperative Excitation and Many-Body Interactions in a Cold Rydberg Gas, Phys. Rev. Lett. **109**, 053002 (2012).

[84] A. W. Glaetzle, M. Dalmonte, R. Nath, C. Gross, I. Bloch, and P. Zoller, Designing Frustrated Quantum Magnets with Laser-Dressed Rydberg Atoms, Phys. Rev. Lett. **114**, 173002 (2015).

[85] J. Qian, L. Zhang, J. Zhai, and W. Zhang, Dynamical phases in a one-dimensional chain of heterospecies Rydberg atoms with next-nearest-neighbor interactions, Phys. Rev. A **92**, 063407 (2015).

[86] T. L. Nguyen, J. M. Raimond, C. Sayrin, R. Cortiñas, T. Cantat-Moltrecht, F. Assemat, I. Dotsenko, S. Gleyzes, S. Haroche, G. Roux, T. Jolicoeur, and M. Brune, Towards Quantum Simulation with Circular Rydberg Atoms, Phys. Rev. X **8**, 011032 (2018).

[87] A. Kshetrimayum, H. Weimer, and R. Orús, A simple tensor network algorithm for two-dimensional steady states, Nat. Commun. **8**, 1291 (2017).

[88] W. Casteels, R. M. Wilson, and M. Wouters, Gutzwiller Monte Carlo approach for a critical dissipative spin model, Phys. Rev. A **97**, 062107 (2018).

[89] D. Huybrechts and M. Wouters, Cluster methods for the description of a driven-dissipative spin model, Phys. Rev. A **99**, 043841 (2019).

[90] R. M. Wilson, K. W. Mahmud, A. Hu, A. V. Gorshkov, M. Hafezi, and M. Foss-Feig, Collective phases of strongly interacting cavity photons, Phys. Rev. A **94**, 033801 (2016).

[91] R. Pathria and P. Beale, *Statistical Mechanics* (Elsevier, Amsterdam, 2011).

[92] N. Shammah, S. Ahmed, N. Lambert, S. De Liberato, and F. Nori, Open quantum systems with local and collective incoherent processes: Efficient numerical simulations using permutational invariance, Phys. Rev. A **98**, 063815 (2018).

[93] Q. Niu and F. Nori, Theory of superconducting wire networks and Josephson-junction arrays in magnetic fields, Phys. Rev. B **39**, 2134 (1989).

[94] W. Metzner, Linked-cluster expansion around the atomic limit of the hubbard model, Phys. Rev. B **43**, 8549 (1991).

[95] S. Schmidt and G. Blatter, Strong Coupling Theory for the Jaynes-Cummings-Hubbard Model, Phys. Rev. Lett. **103**, 086403 (2009).

[96] M. Biondi, S. Lienhard, G. Blatter, H. E. Türeci, and S. Schmidt, Spatial correlations in driven-dissipative photonic lattices, New J. Phys. **19**, 125016 (2017).

[97] A. Biella, J. Jin, O. Viyuela, C. Ciuti, R. Fazio, and D. Rossini, Linked cluster expansions for open quantum systems on a lattice, Phys. Rev. B **97**, 035103 (2018).

[98] T. Prosen, $\mathcal{PT}$-Symmetric Quantum Liouvillean Dynamics, Phys. Rev. Lett. **109**, 090404 (2012).

[99] A. Russomanno, F. Iemini, M. Dalmonte, and R. Fazio, Floquet time crystal in the Lipkin-Meshkov-Glick model, Phys. Rev. B **95**, 214307 (2017).

[100] J. Zhang, G. Pagano, P. W. Hess, A. Kyprianidis, P. Becker, H. Kaplan, A. V. Gorshkov, Z. X. Gong, and C. Monroe, Observation of a many-body dynamical phase transition with a 53-qubit quantum simulator, Nature (London) **551**, 601 (2017).

[101] Z. Davoudi, M. Hafezi, C. Monroe, G. Pagano, A. Seif, and A. Shaw, Towards analog quantum simulations of lattice gauge theories with trapped ions, Phys. Rev. Res. **2**, 023015 (2020).

[102] A. Ramos and C. Cormick, Feasibility of the ion-trap simulation of a class of non-equilibrium phase transitions, Eur. Phys. J. D **73**, 237 (2019).

[103] G. T. Noe II, J.-H. Kim, J. Lee, Y. Wang, A. K. Wojcik, S. A. McGill, D. H. Reitze, A. A. Belyanin, and J. Kono, Giant superfluorescent bursts from a semiconductor magneto-plasma, Nat. Phys. **8**, 219 (2012).

[104] F. Iemini, A. Russomanno, J. Keeling, M. Schirò, M. Dalmonte, and R. Fazio, Boundary Time Crystals, Phys. Rev. Lett. **121**, 035301 (2018).

[105] D. I. Tsomokos, S. Ashhab, and F. Nori, Fully connected network of superconducting qubits in a cavity, New J. Phys. **10**, 113020 (2008).

[106] K. Kakuyanagi, Y. Matsuzaki, C. Déprez, H. Toida, K. Semba, H. Yamaguchi, W. J. Munro, and S. Saito, Observation of Collective Coupling between an Engineered Ensemble of Macroscopic Artificial Atoms and a Superconducting Resonator, Phys. Rev. Lett. **117**, 210503 (2016).

[107] D. Marković, S. Jezouin, Q. Ficheux, S. Fedortchenko, S. Felicetti, T. Coudreau, P. Milman, Z. Leghtas, and B. Huard, Demonstration of an Effective Ultrastrong Coupling between Two Oscillators, Phys. Rev. Lett. **121**, 040505 (2018).

[108] A. Angerer, K. Streltsov, T. Astner, S. Putz, H. Sumiya, S. Onoda, J. Isoya, W. J. Munro, K. Nemoto, J. Schmiedmayer, and J. Majer, Superradiant emission from colour centres in diamond, Nat. Phys. **14**, 1168 (2018).

[109] M. Gärttner, J. G. Bohnet, A. Safavi-Naini, M. L. Wall, J. J. Bollinger, and A. M. Rey, Measuring out-of-time-order correlations and multiple quantum spectra in a trapped-ion quantum magnet, Nat. Phys. **13**, 781 (2017).

[110] C. Bradac, M. T. Johnsson, M. v. Breugel, B. Q. Baragiola, R. Martin, M. L. Juan, G. K. Brennen, and T. Volz, Room-temperature spontaneous superradiance from single diamond nanocrystals, Nat. Commun. **8**, 1205 (2017).

[111] A. Angerer, S. Putz, D. O. Krimer, T. Astner, M. Zens, R. Glattauer, K. Streltsov, W. J. Munro, K. Nemoto, S. Rotter, J. Schmiedmayer, and J. Majer, Ultralong relaxation times in bistable hybrid quantum systems, Sci. Adv. **3**, e1701626 (2017).

[112] R. El-Ganainy, K. G. Makris, M. Khajavikhan, Z. H. Musslimani, S. Rotter, and D. N. Christodoulides, Non-Hermitian physics and PT symmetry, Nat. Phys. **14**, 11 (2018).

[113] M.-A. Miri and A. Alù, Exceptional points in optics and photonics, Science **363**, eaar7709 (2019).

[114] Ş. K. Özdemir, S. Rotter, F. Nori, and L. Yang, Parity–time symmetry and exceptional points in photonics, Nat. Mater. **18**, 783 (2019).

[115] S. Scheel and A. Szameit, $\mathcal{PT}$-symmetric photonic quantum systems with gain and loss do not exist, Europhys. Lett. **122**, 34001 (2018).

[116] T. Prosen, Generic examples of $\mathcal{PT}$-symmetric qubit (spin-1/2) Liouvillian dynamics, Phys. Rev. A **86**, 044103 (2012).

[117] M. van Caspel and V. Gritsev, Symmetry-protected coherent relaxation of open quantum systems, Phys. Rev. A **97**, 052106 (2018).

[118] P. D. Nation, J. R. Johansson, M. P. Blencowe, and A. J. Rimberg, Iterative solutions to the steady-state density matrix for optomechanical systems, Phys. Rev. E **91**, 013307 (2015).

[119] C. Joshi, F. Nissen, and J. Keeling, Quantum correlations in the one-dimensional driven dissipative *xy* model, Phys. Rev. A **88**, 063835 (2013).

[120] P. Kirton and J. Keeling, Superradiant and lasing states in driven-dissipative Dicke models, New J. Phys. **20**, 015009 (2018).

[121] J. Johansson, P. Nation, and F. Nori, QuTiP: An open-source python framework for the dynamics of open quantum systems, Comput. Phys. Commun. **183**, 1760 (2012).

[122] J. Johansson, P. Nation, and F. Nori, QuTiP 2: A python framework for the dynamics of open quantum systems, Comput. Phys. Commun. **184**, 1234 (2013).

[123] B. Olmos, I. Lesanovsky, and J. P. Garrahan, Out-of-equilibrium evolution of kinetically constrained many-body quantum systems under purely dissipative dynamics, Phys. Rev. E **90**, 042147 (2014).

[124] S. Schütz, S. B. Jäger, and G. Morigi, Dissipation-Assisted Prethermalization in Long-Range Interacting Atomic Ensembles, Phys. Rev. Lett. **117**, 083001 (2016).

[125] N. Defenu, T. Enss, M. Kastner, and G. Morigi, Dynamical Critical Scaling of Long-Range Interacting Quantum Magnets, Phys. Rev. Lett. **121**, 240403 (2018).

[126] S. Pappalardi, A. Russomanno, B. Žunkovič, F. Iemini, A. Silva, and R. Fazio, Scrambling and entanglement spreading in long-range spin chains, Phys. Rev. B **98**, 134303 (2018).

[127] J. R. González Alonso, N. Yunger Halpern, and J. Dressel, Out-of-Time-Ordered-Correlator Quasiprobabilities Robustly Witness Scrambling, Phys. Rev. Lett. **122**, 040404 (2019).

[128] R. Khasseh, R. Fazio, S. Ruffo, and A. Russomanno, Many-Body Synchronization in a Classical Hamiltonian System, Phys. Rev. Lett. **123**, 184301 (2019).

[129] B. Buča and T. Prosen, A note on symmetry reductions of the Lindblad equation: transport in constrained open spin chains, New J. Phys. **14**, 073007 (2012).

[130] V. V. Albert and L. Jiang, Symmetries and conserved quantities in Lindblad master equations, Phys. Rev. A **89**, 022118 (2014).
[131] Z. Zhang, J. Tindall, J. Mur-Petit, D. Jaksch, and B. Buča, Stationary state degeneracy of open quantum systems with non-abelian symmetries, arXiv:1912.12185.
[132] B. Baumgartner and H. N., Analysis of quantum semigroups with GKS-Lindblad generators: Ii. general, J. Phys. A: Math. Theor. **41**, 395303 (2008).
[133] R. H. Dicke, Coherence in spontaneous radiation processes, Phys. Rev. **93**, 99 (1954).
[134] R. Bonifacio and G. Preparata, Coherent spontaneous emission, Phys. Rev. A **2**, 336 (1970).
[135] R. Bonifacio, P. Schwendimann, and F. Haake, Quantum statistical theory of superradiance. I, Phys. Rev. A **4**, 302 (1971).
[136] R. Bonifacio and L. A. Lugiato, Cooperative radiation processes in two-level systems: Superfluorescence, Phys. Rev. A **11**, 1507 (1975).
[137] E. M. Chudnovsky and D. A. Garanin, Superradiance from Crystals of Molecular Nanomagnets, Phys. Rev. Lett. **89**, 157201 (2002).
[138] C. Braggio, F. Chiossi, G. Carugno, A. Ortolan, and G. Ruoso, Spontaneous formation of a macroscopically extended coherent state, arXiv:1909.00999.
[139] G. Rainò, M. A. Becker, M. I. Bodnarchuk, R. F. Mahrt, M. V. Kovalenko, and T. Stöferle, Superfluorescence from lead halide perovskite quantum dot superlattices, Nature (London) **563**, 671 (2018).
[140] N. Lambert, C. Emary, and T. Brandes, Entanglement and the Phase Transition in Single-Mode Superradiance, Phys. Rev. Lett. **92**, 073602 (2004).
[141] R. H. Lehmberg, Radiation from an N-atom system. I. General formalism, Phys. Rev. A **2**, 883 (1970).
[142] M. Buchhold, P. Strack, S. Sachdev, and S. Diehl, Dicke-model quantum spin and photon glass in optical cavities: Nonequilibrium theory and experimental signatures, Phys. Rev. A **87**, 063622 (2013).
[143] N. Lambert, Y. Matsuzaki, K. Kakuyanagi, N. Ishida, S. Saito, and F. Nori, Superradiance with an ensemble of superconducting flux qubits, Phys. Rev. B **94**, 224510 (2016).
[144] E. G. Dalla Torre, Y. Shchadilova, E. Y. Wilner, M. D. Lukin, and E. Demler, Dicke phase transition without total spin conservation, Phys. Rev. A **94**, 061802(R) (2016).
[145] M. Gegg and M. Richter, Efficient and exact numerical approach for many multi-level systems in open system CQED, New J. Phys. **18**, 043037 (2016).
[146] N. Shammah, N. Lambert, F. Nori, and S. De Liberato, Superradiance with local phase-breaking effects, Phys. Rev. A **96**, 023863 (2017).
[147] M. Cirio, N. Shammah, N. Lambert, S. De Liberato, and F. Nori, Multielectron Ground State Electroluminescence, Phys. Rev. Lett. **122**, 190403 (2019).
[148] F. Dimer, B. Estienne, A. S. Parkins, and H. J. Carmichael, Proposed realization of the Dicke-model quantum phase transition in an optical cavity QED system, Phys. Rev. A **75**, 013804 (2007).
[149] D. Meiser and M. J. Holland, Steady-state superradiance with alkaline-earth-metal atoms, Phys. Rev. A **81**, 033847 (2010).
[150] K. Baumann, C. Guerlin, F. Brennecke, and T. Esslinger, Dicke quantum phase transition with a superfluid gas in an optical cavity, Nature (London) **464**, 1301 (2010).
[151] J. G. Bohnet, Z. Chen, J. M. Weiner, D. Meiser, M. J. Holland, and J. K. Thompson, A steady-state superradiant laser with less than one intracavity photon, Nature (London) **484**, 78 (2012).
[152] A. E. Niederle, G. Morigi, and H. Rieger, Ultracold bosons with cavity-mediated long-range interactions: A local mean-field analysis of the phase diagram, Phys. Rev. A **94**, 033607 (2016).
[153] J. Gelhausen, M. Buchhold, and P. Strack, Many-body quantum optics with decaying atomic spin states: (γ, κ) Dicke model, Phys. Rev. A **95**, 063824 (2017).
[154] A. Bermudez, L. Tagliacozzo, G. Sierra, and P. Richerme, Long-range Heisenberg models in quasiperiodically driven crystals of trapped ions, Phys. Rev. B **95**, 024431 (2017).
[155] L. Novo, T. Moroder, and O. Gühne, Genuine multiparticle entanglement of permutationally invariant states, Phys. Rev. A **88**, 012305 (2013).
[156] B. S. Chissom, Interpretation of the kurtosis statistic, Am. Statistician **24**, 19 (1970).
[157] K. Binder, Finite size scaling analysis of Ising model block distribution functions, Z. Phys. B: Condensed Matter Quanta **43**, 119 (1981).
[158] K. Binder, Critical Properties from Monte Carlo Coarse Graining and Renormalization, Phys. Rev. Lett. **47**, 693 (1981).